INVITED PAPER

Internal modification of glass by ultrashort laser pulse and its application to microwelding

Isamu Miyamoto · Kristian Cvecek ·
Yasuhiro Okamoto · Michael Schmidt

Abstract Internal modification process of glass by ultrashort laser pulse (USLP) and its applications to microwelding of glass are presented. A simulation model is developed, which can determine intensity distribution of absorbed laser energy, nonlinear absorptivity and temperature distribution at different pulse repetition rates and pulse energies in internal modification of bulk glass with fs- and ps-laser pulses from experimental modified structure. The formation process of the dual-structured internal modification is clarified, which consists of a teardrop-shaped inner structure and an elliptical outer structure, corresponding to the laser-absorbing region and heat-affected molten region, respectively. Nonlinear absorptivity at high pulse repetition rates increases due to the increase in the thermally excited free electron density for avalanche ionization. USLP enables crack-free welding of glass because the shrinkage stress is suppressed by producing embedded molten pool by nonlinear absorption process, in contrast to conventional continuous wave laser welding where cracks cannot be avoided due to shrinkage stress produced in cooling process. Microwelding techniques of glass by USLP have been developed to join glass/glass and Si/glass using optically contacted sample pairs. The strength of the weld joint as high as that of base material is obtained without pre- and post-heating in glass/glass welding. In Si/glass welding, excellent joint performances competitive with anodic bonding in terms of joint strength and process throughput have been attained.

I. Miyamoto (✉)
Osaka University, 2-1, Yamada-Oka, Suita, Osaka 565-0871,
Japan
e-mail: miyamoto-i@ares.eonet.ne.jp

I. Miyamoto · M. Schmidt
Erlangen Graduate School of Advanced Optical Technologies
(SAOT), Paul-Gordon Str. 6, 91052 Erlangen, Germany

K. Cvecek · M. Schmidt
Bayerisches Laserzentrum, Konrad-Zuse Str. 2-6,
91052 Erlangen, Germany

Y. Okamoto
Okayama University, 3-1-1 Thsushimanaka,
Okayama 700-8530, Japan

M. Schmidt
University Erlangen-Nuremberg, Paul-Gordon Str. 6,
91052 Erlangen, Germany

1 Introduction

Ultrashort laser pulse (USLP) has a huge potential in internal modification of transparent material in a wide variety of fields including optics, electronics, electro-optics, MEMS and so on. Davis et al. [1] reported internal modification of bulk glass, demonstrating highly localized and permanent refractive index change is produced using tightly focused femtosecond (fs) laser pulse. Since then a variety of internal modifications of glass have been reported, which include waveguide formation [2–4], waveguide splitter [5, 6], grating [7], 3D-memories [8], selective etching [9], microwelding [10–12] and so on.

Internal modification of glass can be divided into two different regimes of high and low pulse repetition rates. Most of the internal modifications reported in the early stage rely on low repetition rates in the range of kHz. However, the low pulse repetition rates have some disadvantages including higher tendency for defect formation like cracks as well as slow process speed, typically tens of microns per second for waveguide formation, for instance, resulting in longer fabrication time. In contrast, at high

pulse repetition rates of the order of MHz, significantly higher process speeds up to several tens to hundreds of millimeters per second are available with reduced tendency for cracking because the thermal stress caused by local deposition of the laser energy is mitigated by the temperature field produced at high pulse repetition rates.

Schaffer et al. [13] presented a paper showing the advantages of the internal glass modification by USLP at a pulse repetition rate as high as 25 MHz. They reported that the dimension of the modified region becomes much larger than that of the focus volume at high pulse repetition rates due to the effects of heat accumulation, and can be simulated by classical thermal conduction model. Since then plenty of interesting applications by USLP at high pulse repetition rates have been reported, including waveguide formation [14–19], selective etching [20, 21] and microwelding [22–27]. The thermal conduction model was also reported by several authors, confirming the modified volume can be enlarged at higher pulse repetition rates [28] or by uniform preheating of the glass sample [29, 30].

For optimizing the internal modification, understanding of USLP–matter interaction is essential, through which temperature distribution and thereby the quality and the dimension of modification can be evaluated. Miyamoto et al. [31, 32] reported a simulation model that enables the evaluation of the USLP energy distribution absorbed in the bulk glass at high pulse repetition rates. The model also shows the increase in the modified volume is caused not only by the heat accumulation but by the increase in the nonlinear absorptivity at high pulse repetition rates [12, 31, 32]. While the model is applied to the analysis of microwelding process in the present paper, it can be also applied to waveguide formation, selective etching and so on using USLP at high pulse repetition rates.

It is known in existing welding technology that cracks cannot be avoided in local melting of glass having large coefficient of thermal expansion (CTE) due to thermal stress, when CW-laser is used [33–35]. Therefore, the fact that crack-free local melting of glass is realized by USLP without pre- and post-heating was a kind of a mystery for a long time. Recently the mystery has been solved by the new finding [32] that no shrinkage stress is produced in internal local melting by nonlinear absorption process, adding a new page in the history of welding technology.

Among a variety of internal modifications by USLP, microwelding of glass has been drawing special attention, because no reliable procedure exists to join glass pieces, while glass is widely used in different fields. The origin of the advantages is provided by the nonlinear properties of USLP. It is believed that USLP welding glass will open the door to microwelding field in the next generation.

In this paper, recent achievements of nonlinear absorption process at high pulse repetition rates are presented based on the USLP–glass interaction model, which will be

described briefly here because it is detailed in References [31, 32]. USLP is applied to microwelding for joining glass/glass and Si/glass. In microwelding of brittle material, crack-free internal melting is realized by the advantageous feature of the nonlinear absorption process to provide embedded molten pool. It is shown that the embedded molten pool suppresses the shrinkage stress, which is known to be the origin of cracks in conventional CW-laser welding. Another feature of USLP processing is the time-delay of the temperature rise after the laser pulse. High-quality Si/glass weld joint is obtained by suppressing the excess temperature rise at the thin surface layer of Si substrate during the laser pulse, so that the increase in the laser absorption coefficient is suppressed to enable milder heating of Si substrate, resulting in excellent weld quality.
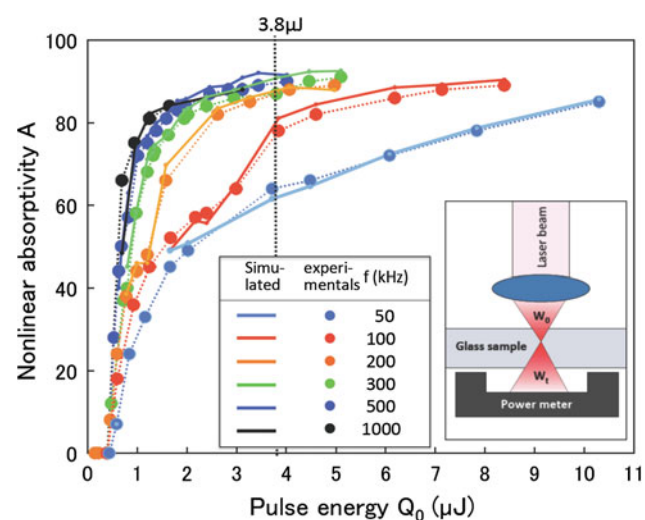
2 Nonlinear absorption process

2.1 Experimental results of internal modification

Internal modification of glass by USLP is strongly dependent on the nonlinear absorptivity. Assuming reflection and scattering from the laser-induced plasma is negligible, the nonlinear absorptivity is given by [12, 23].

$$A_{Ex} = 1 - \frac{Q_t}{Q_0} \frac{1}{(1-R)^2} \qquad (1)$$

where Q_0 is incident laser pulse energy, Q_t transmitted laser pulse energy through the glass sample and R Fresnel reflectivity. Nahen et al. [36] reported that the reflection and the scattering of the laser energy by the plasma in distilled water are negligible at pulse duration τ_p of 30 ps

Fig. 1 Simulated and experimental nonlinear absorptivity plotted vs. pulse energy Q_0 in D263 at different pulse repetition rates f ($\tau_p = 10$ ps, NA 0.55, $v = 20$ mm/s)

Fig. 2 Cross-sections at different pulse energies Q_0 and pulse repetition rates f **a** 50 kHz, **b** 200 kHz and **c** 500 kHz at 20 mm/s in D263. The laser beam was focused at $z_h = 260$ μm shown by *dotted line* ($\tau_p = 10$ ps, NA 0.55, $v = 20$ mm/s)
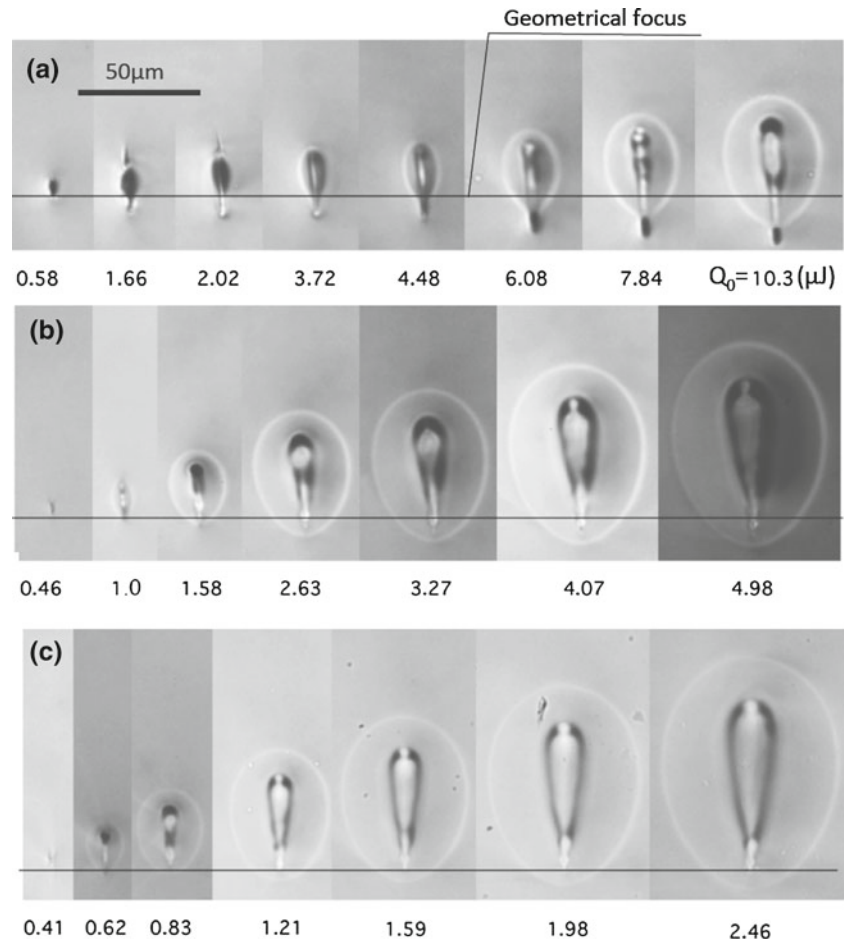

and 8 ns, showing that the above assumption is valid. This is because even if the free electron density exceeds the critical value in the bulk glass, the absorbing plasma with lower electron densities existing in the surrounding area can absorb the reflected laser energy. Thus A_{Ex} of the bulk glass can be experimentally determined by measuring the transmitted pulse energy Q_t below the glass sample (see the inset of Fig. 1). As will be shown later on, this procedure can determine nonlinear absorptivity with accuracy of as small as ±3 %, and thus has been accepted for determining the nonlinear absorptivity [30, 37, 38].

The nonlinear absorptivity in borosilicate glass D263 (Schott) was determined at different pulse energies Q_0 and pulse repetition rates f using 10 ps laser pulses (wavelength $\lambda = 1,064$ nm). In the experiment, the laser beam was focused by an objective lens of NA 0.55 into bulk glass moving at speed v of 20 mm/s at location of $z_h = 260$ μm from the sample surface. The experimental nonlinear absorptivity A_{Ex} is plotted vs. pulse energy at different pulse repetition rates f in Fig. 1. A_{Ex} increases as the energy and the repetition rate of the laser pulse increase.

Figure 2 shows the cross-section of the laser-irradiated samples. The cross-section typically shows a dual-structure

consisting of an elliptical outer structure and a teardrop-shaped inner structure except for the case of lower pulse energies. Geometrical focus shown by the horizontal line was determined at the location of the modified region near the threshold pulse energy. Thus determined geometrical focus agrees with the bottom tip of the inner structure except for higher pulse energies at 50 kHz due to self-focusing and defocusing by electron cloud. While the cross-sectional area increases as the pulse repetition rate increases in accordance with the report by Schaffer et al. [13], Fig. 1 indicates the increase in the cross-sectional area is caused not only by the heat accumulation but by the increase in the nonlinear absorptivity.

Internal melting was also performed in D263 using 400 fs-laser pulses at different translation speeds v ($f = 1$ MHz, $Q_0 = 0.5$ μJ, NA 0.65 and $z_h = 100$ μm), exhibiting basically the same dual-structure as that of 10 ps-laser pulse, as shown in Fig. 3a. Experimental non-linear absorptivity A_{Ex} tends to decrease slightly as the translation speed increases, as shown in Fig. 3b. When A_{Ex} is compared between $\tau_p = 400$ fs and $\tau_p = 10$ ps at the same condition of 0.5 μJ–1 MHz, somewhat higher A_{Ex} is obtained with 400 fs-duration. However, the nonlinear
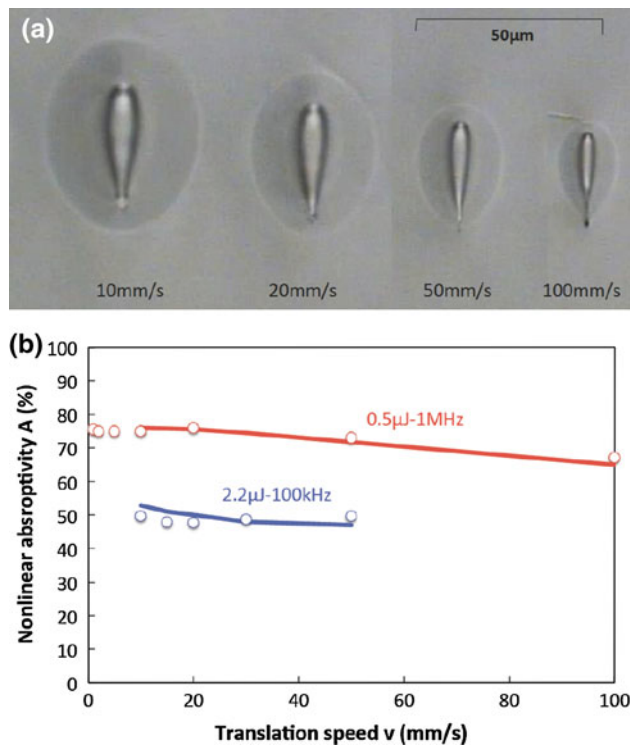
Fig. 3 **a** Cross-sections and **b** nonlinear absorptivity plotted vs. pulse energy Q_0 in D263. *Open circles* and *solid line* correspond to A_{Ex} and A_{Cal}, respectively ($\tau_p = 400$ fs, $f = 1$ MHz, NA 0.65). Focus is located at a depth of $z_h = 100$ μm

absorptivity with two these pulse durations seems to be equivalent at higher pulse energies when considering that $Q_0 = 0.5$ μJ is close to the threshold energy for nonlinear absorption at 10 ps-duration, and that 400 fs-pulses were focused at smaller z_h by larger NA lens. Further study is needed for the detailed comparison.

2.2 Thermal conduction model

2.2.1 Transient temperature distribution

When USLP is focused into transparent material like glass, the laser energy is absorbed by photoionization followed by avalanche ionization,and the laser energy absorbed in thus produced plasma is transferred to the lattice to develop the temperature field. While experimental temperature measurement in the USLP-irradiated bulk glass using time-resolved micro-Raman spectroscopy technique [39] has been published, the temperature measurement at high pulse repetition rates is quite limited [40]. So the temperature field has been analyzed mainly by simulation based on classical thermal conduction model. Then the absorbed laser energy is concerned as an instantaneous heat source, since the laser energy absorbed by the free electrons is transferred to the lattice much faster than thermal diffusion.

In the simulation of the temperature field, the distribution of the absorbed laser energy is a key issue. While the distribution of the laser energy absorbed in the laser-induced plasma has been simulated based on the rate equation for free electrons in distilled water [41–44], the analyses are limited to the single laser pulse.

In this study, an analytical solution for thermal conduction model is developed, which simulates temperature distribution in the moving bulk glass irradiated by tightly focused successive USLP at high pulse repetition rates. The distribution of the laser energy absorbed in the plasma is determined by fitting the simulated isotherm to the experimental modification structure produced in the bulk glass. This approach has an advantage that the absorbed laser energy can be determined straightforward, since the precise temperature distribution is automatically recorded in the bulk glass as the modified structure.

While the simulation model is applied to microwelding of glass in this study, it can be also applied to other thermal modification process at high pulse repetition rates including waveguide formation [14–19], selective etching [20, 21] and so on for simulating distributions of absorbed laser energy, free electron density and the temperature field.

The differential equation of the thermal conduction

$$\frac{\partial^2 T}{\partial x^2} + \frac{\partial^2 T}{\partial x^2} + \frac{\partial^2 T}{\partial x^2} = \frac{1}{\alpha}\frac{\partial T}{\partial t} \tag{2}$$

is satisfied by the solution given by [45].

$$T(x, y, z; t)$$
$$= \frac{Q}{8\{\pi\alpha(t-t')\}^{3/2}} \exp\left\{-\frac{(x-x')+(y-y')+(z-z')}{4\alpha t}\right\} \tag{3}$$

where c is specific heat, ρ density, α thermal diffusivity, Q pulse energy and t time. Equation (3) is known as the temperature due to an instantaneous point source, which gives the temperature at (x, y, z) at time t in an infinite body with initial temperature zero due to the heat Q generated at time $t = t'$ at a point (x', y', z') [45]. Assuming a three-dimensional heat source with arbitrary distribution $q(x', y', z')$ generates instantaneously at a repetition rate of f in the infinite body moving at a speed of v along x-axis, the temperature at (x, y, z) at time t after the generation of Nth pulse is given by

$$T(x,y,z;t) = \frac{1}{8c\rho}\sum_{i=0}^{N-1}\int_{-\infty}^{\infty}\int_{-\infty}^{\infty}\int_{-\infty}^{\infty}\frac{q(x'+v(t+if^{-1}),y',z')}{\{\pi\alpha(t+if^{-1})\}^{3/2}}$$
$$\times \exp\left[-\frac{\{x-x'+v(t+if^{-1})\}^2+(y-y')^2+(z-z')^2}{4\alpha(t+if^{-1})}\right]dx'dy'dz'$$

We assume that Gaussian beam propagates along z-axis in glass sample with the laser spot $\omega(z)$ as shown in Fig. 4. Then the laser spot radius at z is given by [46].

$$\omega(z) = \omega_0 \sqrt{1 + \left(\frac{M^2 \lambda z}{\pi \omega_0^2 n_g}\right)^2}; \quad \omega_0 = \frac{M^2 \lambda}{\pi NA}, \quad (4)$$

where z is distance from the focus along the optical axis, λ wavelength of the laser beam, ω_0 radius of laser spot at $z = 0$, M^2 beam quality factor, NA numerical aperture of focusing optics and n_g refractive index of the bulk glass. Assuming that $w(z)$ is time-averaged absorbed laser power integrated in (x, y) plane, the laser energy absorbed at (x, y, z) per unit volume per pulse $q(x, y, z)$ is given by

$$q(r, z) = \frac{2w(z)}{\pi \omega^2(z) f} \exp\left\{-\frac{2r^2}{\omega^2(z)}\right\}; \quad 0 \le z \le l, \quad (5)$$

where $r = \sqrt{x^2 + y^2}$. When $q(r, z)$ generates instantaneously at a repetition rate of f in an infinite body, which moves transversely to the laser beam at a constant speed of v, the temperature at (x, y, z) at time t after the deposition of Nth pulse is given by

$$T_N(x, y, z; t) = \frac{1}{\pi c \rho f} \sum_{i=0}^{N-1} \frac{1}{\sqrt{\pi \alpha (t - if^{-1})}} \int_0^l \frac{w(z')}{\omega^2(z') + 8\alpha(t - if^{-1})}$$
$$\times \exp\left[-\frac{2\left\{(x + v(t - if^{-1}))^2 + y^2\right\}}{\omega^2(z') + 8\alpha(t - if^{-1})} - \frac{(z - z')^2}{4\alpha t}\right] dz' \quad (6)$$

In this model, it is assumed that thermal properties of glass are independent of temperature, for simplicity.

2.2.2 Simulation of steady isotherm in modified structure

In order to simulate $T_N(x, y, z; t)$ using Eq. (6), the spatial distribution of the absorbed laser energy along z-axis $w(z)$ or $q(r, z)$ given by Eq. (5) has to be determined. In order to determine $w(z)$, a line heat source model with continuous heat delivery is introduced where all the deposited energy $q(r, z)$ is concentrated on the infinitesimally thin line along z-axis as shown in Fig. 4. Then the temperature distribution due to the line heat source is written in a form [45].

$$T(x, y, z) = \frac{1}{4\pi K} \int_0^l \frac{w(z')}{s} \exp\left\{-\frac{v}{2\alpha}(x + s)\right\} dz' + T_0, \quad (7)$$

where $s^2 = x^2 + y^2 + (z - z')^2$ and K is thermal conductivity. Such a simple model can be used in simulating isotherm of the molten region instead of Eq. (6), because the temperature rise at locations apart from the heat source can be spatially and temporally averaged. The maximum cycling temperature in the moving heat source is reached at the location of x where $dT/dx = 0$,
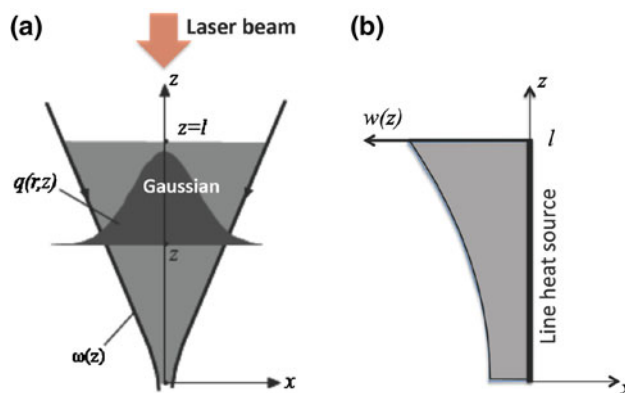
Fig. 4 **a** Instantaneous Gaussian heat source with radius of $\omega(z)$ and energy of $q(r, z)$ at repetition rate of f. **b** Line heat source of continuous heat delivery with average intensity distribution $w(z)$. The focus is at $z = 0$

$$\int_0^l \frac{w(z')}{s} \exp\left\{-\frac{v}{2\alpha}(x + s)\right\} \left\{\frac{x}{r^3} - \frac{v}{2\alpha}\left(\frac{x}{r} - 1\right)\right\} dz' = 0 \quad (8)$$

The isotherm of the maximum cycling temperature is determined by substituting the solution of Eq. (8) into Eq. (7).

### 2.3 Characteristic temperature of the outer structure

In this study, $w(z)$ is determined by fitting the simulated isotherm of Eq. (7) to the experimental modified structure. Then the characteristic temperature of the modified structure has to be known.

Figure 5a shows cross-sections of overlap-welded joint with a sample pair of optically contacted D263. The welded sample was slightly etched by HF to make the interface line visible, since the optically contacted interface line is very thin. It is seen that joining of two glass pieces is accomplished within the outer structure. Figure 5b shows the cross-section of the multipass weld bead in D263. Two glass pieces are joined together in the outer structure again. Figure 5c shows the overlap-weld joint in fused silica. Two glass pieces are joined together in the modified region in fused silica, while the sample is broken by chance at location apart from the interface during cutting and polishing process for sample analysis. We should note that no inner structure is observed in fused silica unlike the case of borosilicate glass. The inner structure is produced in borosilicate glass, because network modifiers are enriched around the laser-absorbed region [47] as will be described later. In fused silica no network modifiers are contained, and hence the modified structure in fused silica corresponds to the outer structure in borosilicate glass.

Fig. 5 Cross-sections of overlap-welded glass sample with optical contact. **a** D263, sample was lightly etched by HF after welding to show the interface clearly. **b** Multi-pass welding of D263. **c** Fused silica, note that the sample was broken during sample preparation of cross-section
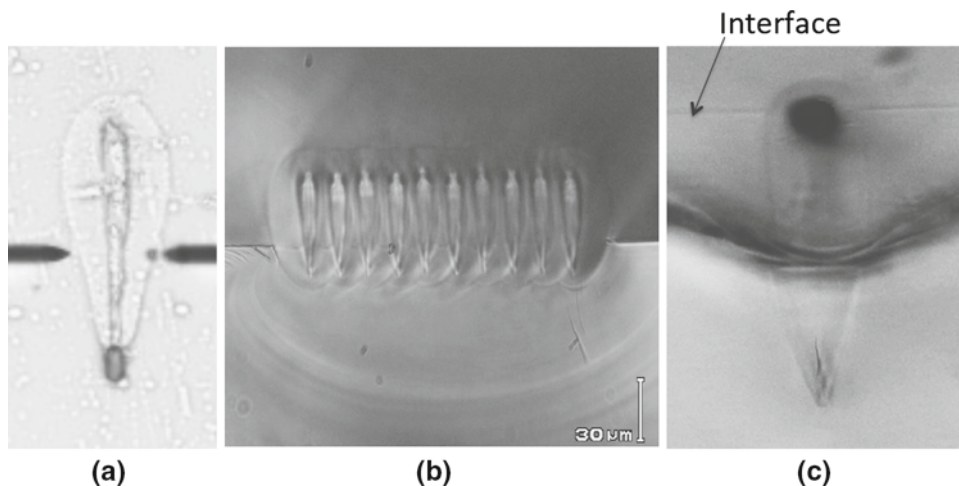
Fig. 6 Cross-section of borosilicate glass (Corning 0211) overlap-welded with femtosecond laser pulses ($\tau_p = 360$ fs, 10 mm/s, 0.7 μJ–1 MHz). **a** Transmission and **b** reflection images of weld region [48]
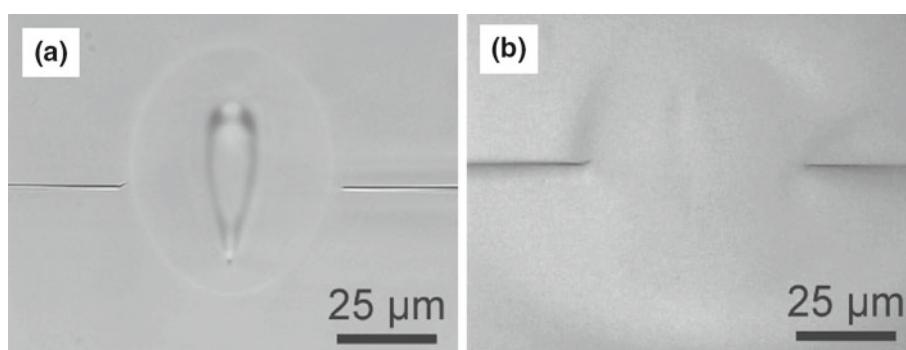
Dual-structured modification of the welded joint can be also found in literature. Figure 6 shows the cross-section of borosilicate sample pair (Corning 0211) made by focused 360 fs-laser pulses reported by Bovatsek et al. [48]. The figure clearly shows two glass pieces are joined together in the outer region. The interface line is observed clearly without etching, because joining was realized by chance without optical contact in this case, although optical contact is recommended for successful welding of glass pieces [24, 27, 49] as will be discussed in Sect. 3.2.3. Based on the above results, it is concluded that the outer structure is the molten region where forming temperature with a viscosity of 10^4 dPas is reached.

Table 1 shows some examples of the characteristic temperature of the outer structure corresponding to the forming temperature. Eaton et al. [28] estimated the temperature of the outer region in AF45 (Schott) to be 1,225 °C, which agrees with the forming temperature of AF45. Thus the characteristic temperature of the outer structure of D263 is estimated to be $T_{out} = 1,051$ °C.

The characteristic temperature of the modified structure of borosilicate glass B270 (Schott) is also speculated from the relaxation time after applying stress based on visco-elastic model [50], and is estimated to be as low as 560 °C [29, 30], whose viscosity corresponds to 10^{11} dPas. The speculated viscosity is too high to fill the gap to accomplish

Table 1 Characteristic temperature of the outer structure

Glass	Temperature corresponding to 10^4 dPas (°C)
0211 (Corning)	1,008
B270 (Schott)	1.033
D263 (Schott)	1,051
AF45 (Schott)	1,225
Borofloat 33 (Schott)	1,280

welding, suggesting the viscoelastic model provides significantly lower temperature.

2.4 Simulation of isothermal lines

2.4.1 fs-laser pulses

$w(z)$ is determined by fitting the isotherm of T_{out} simulated by Eq. (7) to the contour of the outer structure. In order to minimize the number of the parameters to be determined in the fitting routine, simplest monotonically increasing function $w(z)$.

$$w(z) = az^m + b; \quad 0 < z < l, \tag{9}$$

is assumed where *a, b, m* and *l* are positive constants. Here $m = 2$ is assumed when considering that the beam spot

radius is proportional to z at locations apart from the focus in Eq. (4).

In Fig. 7, the *green lines* show the distribution of $w(z)$ determined by fitting the simulated isotherm of $T_{out} = 1{,}051$ °C to the experimental outer structures with 400 fs-laser pulses at different translation speeds (see Fig. 3; $Q_0 = 0.5$ µJ, $f = 1$ MHz). The isotherm of $T_{out} = 1{,}051$ °C plotted with the *blue line* shows nearly perfect fitting to the outer structure, and the inner structure also agrees with the isotherm of $T_{in} \approx 3{,}500$ °C shown with the *red line*. It is noted that the simulated length of the

laser absorption region l and the focus position agree well with the experimental length of the inner structure and the geometrical focus, respectively.

2.4.2 ps-laser pulses

Figure 8a shows the cross-sections of the experimental modified structure with 10 ps-laser pulses at different pulse repletion rates ($Q_0 = 1.67$ µJ, $v = 20$ mm/s). The isotherm of $T_{out} = 1{,}051$ °C is fitted to the contour of the outer structure as shown in Fig. 8b. At pulse repetition

Fig. 7 Simulated isotherms of T_{in} and T_{out} along with $w(z)$ in D263 produced by 400 fs laser pulses ($\lambda = 1{,}045$ nm) corresponding to Fig. 3 at v (mm/s) **a** 10, **b** 20, **c** 50 and **d** 100

(a) 10mm/s   **(b)** 20mm/s   **(c)** 50mm/s   **(d)** 100mm/s
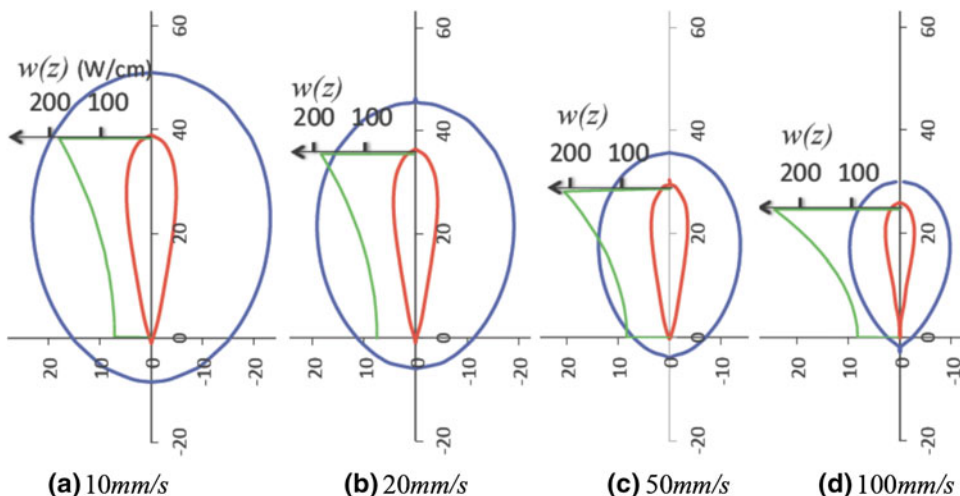
Fig. 8 a Cross-sections and **b** simulated isothermal lines of T_{out} (*blue line*) and T_{in} (*red line*) obtained by 10 ps-laser pulses (NA 0.55, D263, $m = 2$) at different pulse repetition rates

f(kHz)=50   100   200   300   500
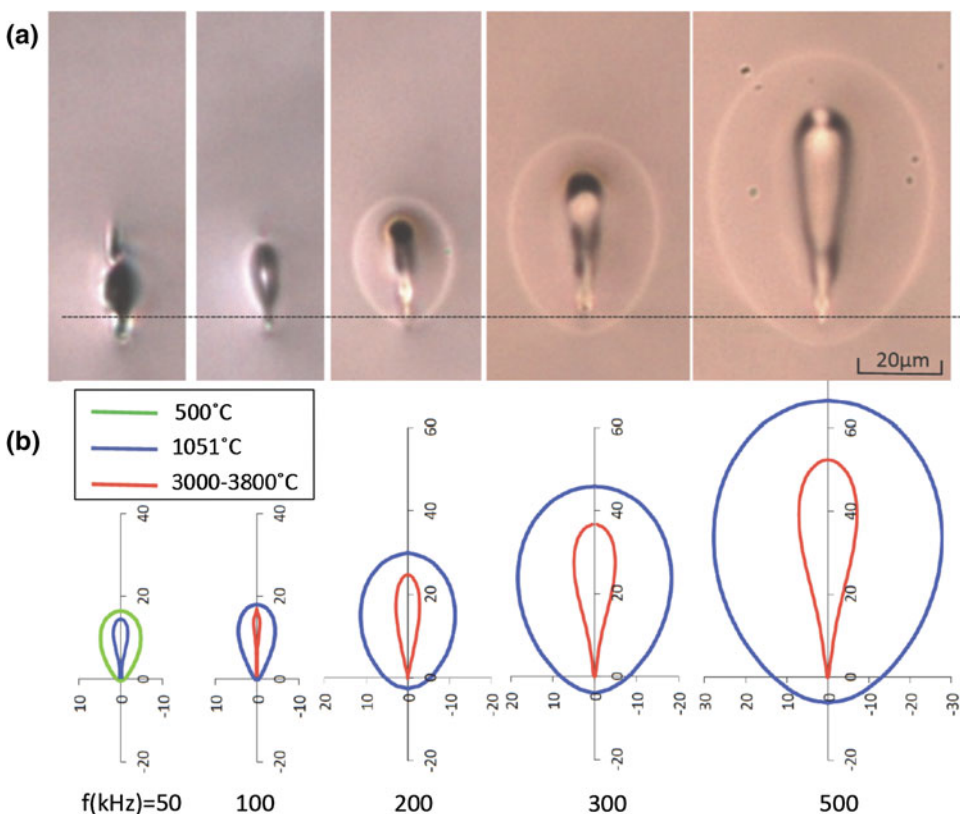
rates of $f = 200–500$ kHz where the dual-structure is clearly observed, the isotherm of $T_{out} = 1,051$ °C agrees almost perfectly with the contour of the experimental outer structure again. It is also seen that the simulated focus position and the isotherms $T_{in} = 3,500 \pm 300$ °C agree with the geometrical focus and the inner structure, respectively.

At lower repetition rates of 50 and 100 kHz, the isotherm was simulated using A_{Ex} (Fig. 1), which corresponds to the integration of $w(z)$ from 0 to l in Eq. (7), since the dual-structure cannot be observed. At 100 kHz, the isotherm of 1,051 °C agrees approximately with the contour of the modified region. At 50 kHz, however, it occupies only the narrow region near the laser beam axis, and the contour of the modified region (green line) was as low as approximately 500 °C, as seen in Fig. 8b.

2.4.3 Simulation of nonlinear absorptivity

The average laser power absorbed in the bulk glass is given by the integration of $w(z)$ in $0 < z < l$, and thus nonlinear absorptivity A_{Cal} is given by

$$A_{cal} = \frac{W_{ab}}{fQ_0} = \frac{1}{fQ_0} \int_0^l w(z)\mathrm{d}z \qquad (10)$$

where Q_0 is incident laser pulse energy and f pulse repetition rate. The nonlinear absorptivity A_{Cal} simulated by Eq. (10) is plotted with the solid lines in Fig. 1, showing excellent agreement with the experimental value of A_{Ex}. The accuracy of the simulation can be estimated from the ratio of A_{Cal}/A_{Ex}, as shown in Fig. 9. The value A_{Cal}/A_{Ex} ranges in a narrower region of 1 ± 0.03, when the data with the single-structure corresponding to $W_{ab} \leq 200$ mW are excluded. Based on Fig. 9, it is concluded that the uncertainties of A_{Cal} and A_{Ex} are estimated to be less than ± 0.03, because A_{Cal} and A_{Ex} are determined based on different physical basis, and the errors are accumulated in calculating the ratio of A_{Cal} and A_{Ex}.

2.5 Simulation of transient temperature

2.5.1 Transient temperature distribution on laser axis

While the line heat source model given by Eq. (7) is the excellent approximation in simulating the isotherm for the outer structure, the temperature on the laser axis cannot be simulated by Eq. (7), and has to be simulated by Eq. (6).

Figure 10 shows the temperature variation $T_N(0, 0, z; 0)$ at $Q_0 \approx 3.8$ μJ on the laser beam axis near the focus ($z = 2.5$ μm) and at the middle of the inner structure ($z = l/2$), simulated by Eq. (6) for $f = 50$ kHz and
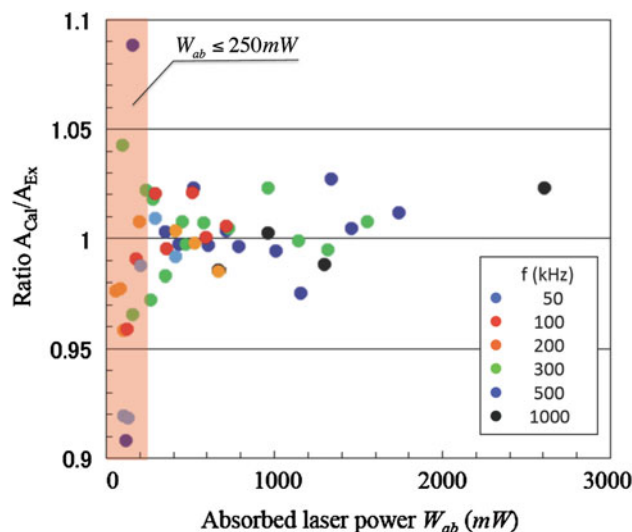
Fig. 9 Ratio of A_{Cal}/A_{Ex} plotted vs. average absorbed laser power W_{ab} in D263 ($K = 0.0093$ W/cm K). A_{Cal}/A_{Ex} ranges in a narrow region of 1 ± 0.03 in dual-structured modification. Data of A_{Cal} and A_{Ex} are shown in Fig. 1

$f = 300$ kHz. The horizontal axis shows the number of laser pulse in logarithmic scale. The temperature variation in each pulse $T_N(0, 0, z; t)$ is plotted until 12th pulse, and thereafter only the base temperature $T_{NB}(z) = T_{N-1}(0, 0, z; \tau)$, which corresponds to the temperature just before the impingement of Nth pulse, is plotted ($\tau = 1/f$).

The temperature at $z = 2.5$ μm rises instantaneously up to $T_{NP}(z) = T_N(0, 0, z; 0)$ just after the impingement of the Nth pulse, and is cooled down to the base temperature $T_{NB}(z) = T_N(0, 0, z; \tau)$ by thermal diffusion between pulses, producing a large amplitude of the temperature change. The base temperature $T_{NB}(z)$ increases pulse by pulse due to heat accumulation. As the pulse repetition rate f increases, $T_{NB}(z)$ increases faster, reaching higher temperature at steady state $T_{SB}(z) = T_{NB}(0, 0, z; \tau); (N \to \infty)$, because cooling time between pulses is shorter. This results in a large difference in the steady value of $T_{BS}(z)$ between 50 and 300 kHz. While the steady base temperature $T_{SB}(z)$ at $z = 2.5$ μm is approximately 800 °C at 50 kHz, the value at 300 kHz reaches as high as approximately 3,000 °C, despite the fact that the temperature rise at each pulse $\Delta T(z) = T_{NP}(z) - T_{NB}(z)$ is smaller at 300 kHz because more laser energy is consumed in the longer and more absorbing plasma. The number of laser pulse N_S for $T_{NB}(z)$ to reach steady temperature $T_{BS}(z)$ increases in proportion to the pulse repetition rate; $N_S \approx 500$ pulses at 50 kHz and $N_S \approx 3,000$ pulses at 300 kHz.

Heat accumulation becomes also significant as the laser spot radius increases, because the cooling rate is slower at larger spot radius due to milder temperature gradient produced around the laser spot. At 300 kHz, for instance,

Fig. 10 Transient temperature simulated on the laser beam axis at $z = 2.5$ μm and $z = l/2$ at 20 mm/s at pulse repetition rates of **a** 50 kHz ($Q_0 = 3.72$ μJ, $l = 22$ μm) and **b** 300 kHz ($Q_0 = 3.9$ μJ, $l = 72$ μm)
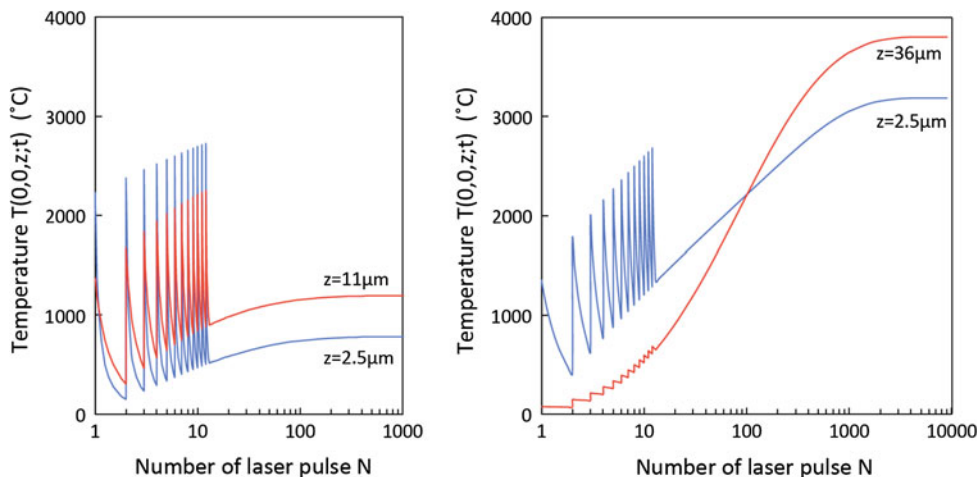
while ΔT at $z = 2.5$ μm is as high as $\Delta T = 1,350$ °C, the steady temperature of $T_{SB}(z)$ is 3,180 °C. However, higher steady temperature of $T_{SB}(z) \approx 3,800$ °C is reached at $z = l/2$, although ΔT is as small as approximately 75 °C. This is because the laser spot size at $z = l/2$ is much larger than at $z = 2.5$ μm. The similar result is also found at 50 kHz; higher $T_{SB}(z) \approx 1,200$ °C is reached at $z = l/2$ although $\Delta T \approx 1,370$ °C is smaller at $z = l/2$. The fact that steady temperatures of $T_{BS}(z)$ at 50 kHz for both $z = 2.5$ μm and $z = l/2$ are much lower than those at 300 kHz is caused not only by longer cooling time but by the fact that the laser spot size in laser absorption region at 50 kHz is much smaller than that of 300 kHz.

$T_B(z)$ plays important roles in determining nonlinear absorptivity and the tendency for cracking, because the free electron density and the ductility of the bulk glass depend on the temperature of the bulk glass when the laser pulse impinges, respectively (see Sects. 2.6 and 3.2).

2.5.2 Steady temperature distribution along laser axis

Figure 11 shows the distribution of $T_{SB}(z)$ and $T_{SP}(z)$, which correspond respectively to

$$T_{SB}(z) = \lim_{N \to \infty} T_N(0, 0, z; \tau),$$
$$T_{SP}(z) = \lim_{N \to \infty} T_N(0, 0, z; 0). \tag{11}$$

The temperature rise per pulse $\Delta T(z)$ is given by

$$\Delta T(z) = T_{SP}(z) - T_{SB}(z). \tag{12}$$

The curve of $T_{SB}(z)$ shows its maximum near the middle of the inner structure along z-axis, as the result of the competition between increase in cooling rate and temperature rise $\Delta T(z)$ as the focus is approached. In this study, $T_{SB}(z)$ and $\Delta T(z)$ are used as the measures for analyzing nonlinear absorptivity and the tendency for cracking as discussed in Sects. 2.6 and 3.2.
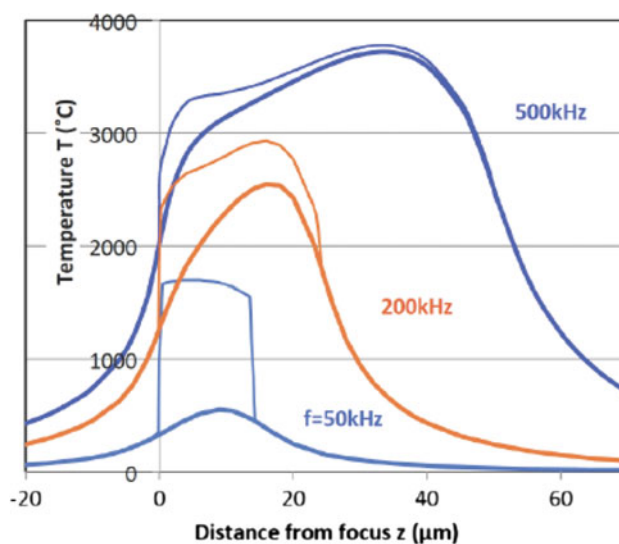

Fig. 11 Distribution of $T_{SB}(z)$ and $T_{SP}(z)$ along z-axis plotted by *thick and thin lines*, respectively, at $f = 50$, 200 and 500 kHz ($N \to \infty$)

2.6 Characterization of inner structure

2.6.1 Laser absorption in inner structure

The steady base temperature $T_{SB}(z)$ ($N \to \infty$) on the laser axis at $z = 2.5$ μm and $z = l/2$ is simulated at different pulse repetition rates of $f = 50$ kHz–1 MHz at pulse energy of $Q_0 = 3.8 \pm 0.18$ μJ (along dotted line in Fig. 1). Figure 12a shows the simulated $T_{BS}(z)$ plotted vs. f. Both curves show basically similar behavior except that $T_{BS}(z)$ increases faster in $z = l/2$ with increasing pulse repetition rate. The temperature at 50 kHz is as low as 800–1,000 °C, indicating that heat accumulation is less effective and hence the laser pulses impinge always in rather "cold" bulk glass. As the pulse repetition rate increases, $T_{BS}(z)$ increases rapidly, reaching approximately 4,000 °C or even higher.

Fig. 12 a Temperature $T_{SB}(z)$ attained at steady condition ($N \to \infty$), and **b** thermally excited free electron density $n_{eB}(0, 0, z; \tau)$ at $z = 2.5$ μm and $z = l/2$. ($Q_0 = 3.9 \pm 0.18$ μJ, $E_g = 3.7$ eV, $v = 20$ mm/s)
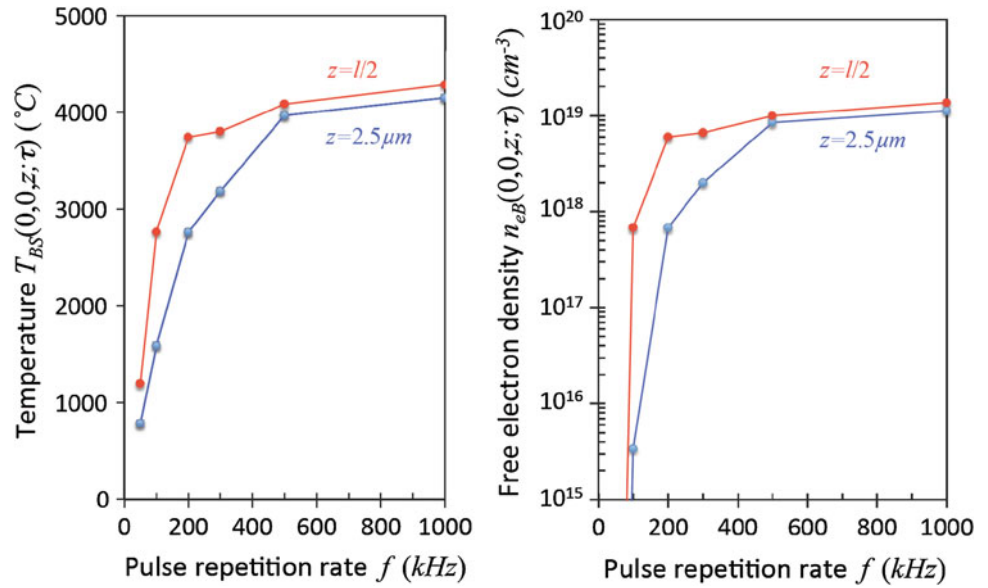
The free electron density thermally excited to the conduction band at temperatures plotted in Fig. 12a is simulated, assuming that molecules are thermalized [51] for the base temperature $T_{BS}(z)$ where the band gap energy of D263, $E_g = 3.7$ eV, determined by a Tauc plot of optical transmission spectroscopy data [52], was used. Figure 12b shows the free electron density calculated at the temperatures of $T_{BS}(z)$ at $z = 2.5$ μm and $z = l/2$ plotted vs. pulse repetition rate f. At 50 kHz, the thermally excited free electron density at $z = l/2$ is so small that negligible number of free electrons is found in the laser-absorption region, suggesting avalanche ionization is seeded solely by multiphoton ionization. This result is supported by the fact that the laser intensity at the upper edge of the inner structure at 50 kHz is nearly equal to the threshold intensity for multiphoton ionization [31, 53, 54]. As the pulse repetition rate f increases, the corresponding free electron density $n_{eB}(0, 0, z; \tau)$ at $z = l/2$ increases, and reaches nearly constant value of $\approx 10^{19}$/cm³, which is high enough to seed the avalanche ionization without seeding by multiphoton ionization [41]. This result suggests that the avalanche ionization can be maintained without seeding the free electrons by multiphoton ionization. The free electron density near the focus ($z = 2.5$ μm) also increases with increasing pulse repetition rate reaching up to $\approx 10^{19}$/cm³, nearly equal to that of $l/2$ at pulse repetition rates $f \geq 500$ kHz.

2.6.2 Formation process of dual structure

Figure 7 shows that the simulated length of the absorption region l and the focus position with 400 fs-pulses agree well with the length of the experimental inner structure l_{in} and the geometrical focus, respectively. Figure 13 compares l and l_{in} in more detail with 10 ps-laser pulses at different
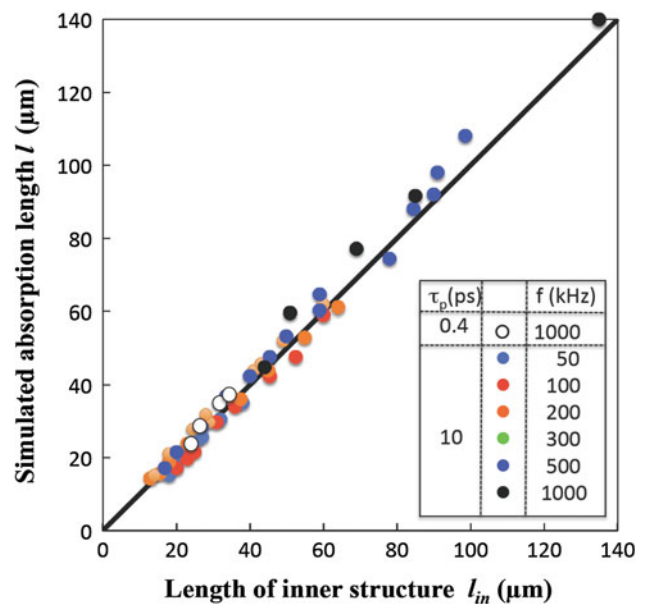
Fig. 13 Correlation of length between simulated laser absorption l and experimental inner structure l_{in} with 400 fs- and 10 ps-laser pulses at different pulse repetition rates and pulse energies

pulse energies and pulse repetition rates where the dual-structure is produced. In this figure data corresponding to 400 fs-laser pulse are also plotted. It is seen that l agrees well with l_{in} independently of τ_p, Q_0, f and v, leading to the conclusion that the laser energy is absorbed in the inner structure. It is also confirmed with 10 ps-laser pulse that the simulated focus position coincides with the geometrical focus at different pulse energies and pulse repetition rates including more than 60 data examined in this study.

Figure 14 shows l plotted vs. averaged value of the absorbed laser power W_{ab} at different values of Q_0 and
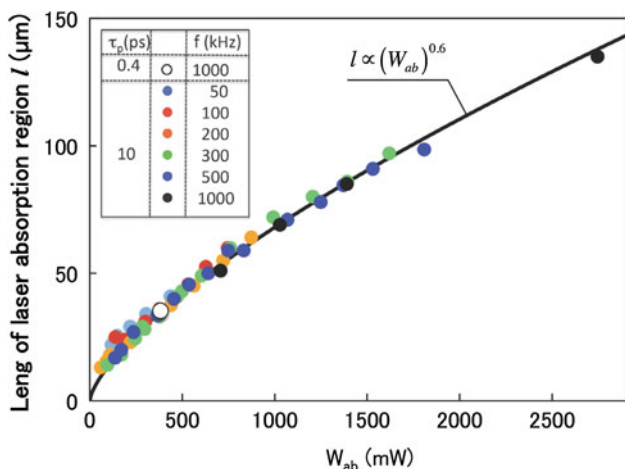
Fig. 14 Simulated absorption length l plotted vs. average absorbed laser power W_{ab} at different pulse energies and pulse repetition rates with 10 ps-laser pulses in D263. *Open circle* corresponds to the value of 400 fs-laser pulse (0.5 μJ–1 MHz)

f using 10 ps-laser pulses at $v = 20$ mm/s with NA 0.55 where self-focusing conditions are excluded. A data point of 400-fs pulse (1 MHz–0.5 μJ) using nearly the same NA of 0.65 at $v = 20$ mm/s is also plotted in the figure. Interestingly all the data fall on a single line, which is approximated by

$$l(W_{ab})^n; \quad \text{where } n \approx 0.6 \tag{13}$$

with very small data scattering independently of τ_p, Q_0 and f. This suggests that the absorbable laser energy in a given length of the inner structure is limited, and that the length of the inner structure has to extend toward the laser source as the absorbed laser energy increases. Figure 14 also shows that the effect of τ_p, Q_0 and f on the absorbable laser power is the same. This means the absorption process is

linear, suggesting the laser absorption is dominated by avalanche ionization at high pulse repetition rates.

The longest inner structure obtained in this study was approximately 140 μm at a condition of 3.14 μJ–1 MHz. In this condition, the laser intensity at the top edge of the inner structure is estimated to be approximately 10^{10} W/cm² , which is approximately two orders smaller than the threshold intensity of multiphoton ionization [53, 54], suggesting the avalanche ionization occurs without seed electrons by multiphoton ionization.

Figure 15 schematically shows the formation process of the dual-structure at high pulse repetition rates. When USLP is tightly focused into the bulk glass, the laser energy is absorbed by multiphoton ionization followed by avalanche ionization to produce plasma in the focus volume. As the number of the laser pulse increases, the laser-absorption region expands toward the laser source to produce a plasma column due to the accumulation of the laser energy absorbed by avalanche ionization at the top edge of the absorption region. The laser-absorbing plasma column corresponds to the inner structure where the free electron density is very high, and is estimated to be of the order of 10^{19}/cm³. Then the molten region corresponding to the outer structure is produced by the thermal diffusion from the inner structure. A point-like plasma with the focus volume size produced by the first laser pulse is converted into the longer plasma column, making the focus adjustment easier in overlap welding, for instance.

It is suggested inner structure is visible because of the following process. When glass is locally heated to high temperature by USLP, all the bonds linking the network modifiers or the network formers are broken in molten glass at high temperature [47]. Various kinds of ions diffuse away from the laser-absorption region to the cooler periphery

Fig. 15 Internal modification process to produce dual-structure by USLP at high pulse repetition rates. Outer structure (molten region) is produced by thermal conduction from inner structure where laser energy is absorbed by avalanche ionization (*HAZ* heat affected zone)
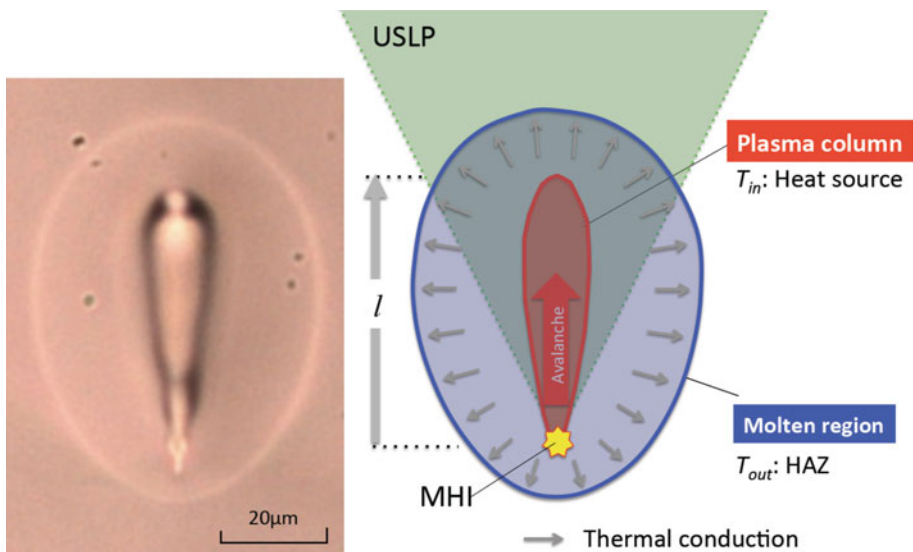
region. The diffusion coefficient of these network modifiers are generally much larger than that of the network formers, so that the network modifiers are enriched around the laser-irradiated region to produce ring-shaped structure in a plane perpendicular to the laser axis [47, 55], making the inner structure visible. This is consistent with the fact that no inner structure is produced in glass having no network modifiers like fused silica as seen in Fig. 5c.

Very recently Sun et al. [56] reported an interesting numerical model to study the internal modification in bulk borosilicate glass irradiated by 10 ps-laser pulses at high repetition rates. In this simulation, plasma formation, nonlinear energy deposition, temperature distribution and modifications are analyzed based on transport equation of laser pulse propagation, a rate equation of the temporal evolution of free electron density and thermal conduction equation. Their simulation is compared with our experimental and simulated results [31, 32]. The model shows that the characteristic temperatures of the inner and outer structures, nonlinear absorptivity and the inner structure size are in good agreement with our results. They define the inner structure is the electronically damaged zone caused by high-density free electrons.

Here we should clarify what the term "nonlinear absorption" in internal modification by USLP implies, since above results indicate that at high pulse repetition rates avalanche ionization governs the breakdown dynamics much more strongly than the case of single pulse, and especially at locations apart from the focus position the seed electrons for avalanche ionization are totally provided by thermal excitation to the conduction band. It is also suggested even a possibility that the laser-induced plasma can be sustained without multiphoton ionization. Nevertheless, however, the multiphoton ionization is still needed at least to start ionization even at high pulse repetition rates. This is qualitatively similar to the case of single 100 fs-laser pulse where breakdown process is dominated by the multiphoton ionization until approximately the laser pulse peak, thereafter the avalanche ionization starts to govern the breakdown dynamics to produce much more free electrons than multiphoton ionization [40]. Thus we should refer to the absorption that needs multiphoton ionization for providing the initial seed electrons as nonlinear absorption.

3 Applications to microwelding

3.1 Background

Although glass is widely used in a variety of industrial fields, joining of glass is still a challenging technology at the moment. While adhesive bonding is widely used in industry for joining glass pieces [57, 58], it has disadvantages of limited heat and chemical durability and low mechanical strength. These disadvantages can be overcome by welding using laser beam, because monolithic joint with high mechanical strength is available. However, laser welding of glass is not easy, since cracks are easily developed by local heating due to its brittle property at room temperature.

Two contrastive lasers, continuous wave (CW) and ultrashort pulse lasers, can be used for modification or processing of glass. CW-laser welding of glass was first reported by Arata et al. [33] where the laser energy is deposited into vapor-filled capillary called *keyhole* based on the similar principle to metal welding [59]. In CW-laser welding, the molten pool always contains free surface, since the laser energy is deposited from the surface of the glass pieces by linear absorption process. Then crack-free welding of glass is possible only with the glass having small CTE like fused silica [33], because tensile stress is produced by the shrinkage of the solidified region in cooling process. While several interesting applications in CW-laser welding of fused silica have been reported [60, 61], crack-free welding is not possible with glass having large CTE.

While a variety of internal modification procedures of bulk glass [1–9] have been developed, nobody imagined USLP can be used for welding in the early period of USLP processing history, because non-thermal features in modification process were much emphasized at that time. Meanwhile the contribution of the thermal effects was reported by several authors in the internal modification. For instance, Watanabe et al. [62] reported a unique experiment where voids formed by tightly focused IR fs laser pulses can be moved and merged in bulk silica glass, suggesting the glass around the void is melted. Schaffer et al. [13] reported that the dimension of the modified region can be much larger than focus volume due to heat accumulation effect at high pulse repetition rates, and can be simulated by thermal conduction model. These experiments suggest that the laser energy absorbed by free electrons can be used to melt bulk glass for welding purpose. Actually it was demonstrated that the molten pool is produced without cracks in borosilicate glass by clear SEM photographs, when 10 ps laser pulses are tightly focused near the rear surface of the glass plate [12].

First microwelding of glass using USLP was reported in 2005 by Tamaki et al. [10] in fused silica using 130-fs laser pulses. Since then several papers on USLP welding of glass have been published from the same group, including welding of dissimilar glasses [11], and glass-to-semiconductor [22]. In these early investigations on glass welding by USLP, sample pairs of flat-to-convex geometry were used for overlap welding with applying mechanical force to provide contact between the glass pieces. However, the resulting joint strength was as low as only 10–20 % of the

base material's strength, because the mechanical force applied to the point-contact geometry in the sample preparation can produce undesirable residual stress or even microcracks.

Cvecek et al. [49] reported that the strength of the weld joint is significantly increased to the value much higher than reported values [10, 11, 22] by adopting optical contact [63, 64] for preparing sample pairs in overlap welding. Miyamoto et al. [24] reported that the mechanical strength of weld joint as high as that of the virgin glass can be reached using optically contacted sample pairs. Since then optical contact is widely used in USLP welding for joining fused silica [25, 26, 65] and borosilicate glass [27, 66], providing excellent joint strength.

Among a wide variety of internal modifications using USLP, microwelding of glass is one of the most promising applications, because cracks could not be prevented in welding of glass having large CTE using CW-laser. Curiously, however, no papers have been published to account for the mechanism of crack-free welding of glass using USLP. Miyamoto et al. [32] recently clarified that the mechanism of crack-free USLP welding of glass is closely related to nonlinear absorption process based on thermal stress model. The model indicates that shrinkage stress, which is the origin of cracking in conventional CW-laser welding in cooling process, can be suppressed when the molten pool has no free surface.

Two mechanisms are utilized in USLP welding of glass. First is nonlinear absorption process to realize internal melting of bulk glass, which enables crack-free glass-to-glass welding to be discussed in Sects. 3.2 and 3.3. Second is the time-delay of temperature rise in USLP processing,

by which the increase in the absorption coefficient of the laser beam in Si during laser pulse is suppressed to make heating of Si substrate milder, and is utilized in welding of Si-to-glass to be described in Sect. 3.4.

## 3.2 Crack-free conditions in USLP welding

### 3.2.1 Thermal stress model in laser welding of glass

Here the thermal stress induced in laser welding process of glass is qualitatively analyzed based on a simple thermal stress model. The model consists of bar A and bar B, which correspond to the laser-heated region and the surrounding region, respectively, and are connected to the rigid body as shown in Fig. 16 [34, 35]. Normally cracks are developed when tensile stress exceeds the strength of material, since tensile strength is much smaller then compressive strength.

In the model, it is assumed that glass is deformed freely without mechanical force at temperatures higher than melting temperature T_M, and that the glass has no ductility at temperatures below T_M, for simplicity. In the thermal stress model, T_M is so called *mechanically* melting temperature, which corresponds to softening temperature T_{soft}.

Tensile stress is produced in bar B in heating process (i), since the thermal expansion of bar A is constrained by colder bar B. In CW-laser welding (Fig. 16a), however, no cracks are produced in bar B even if large tensile stress is produced, because bar B gains ductility by the temperature rise due to the thermal conduction from bar A in the heating process. When bar A is melted, all the stress is released and the length of bars A and B becomes equal, due to plastic deformation of the molten region (ii), since

Fig. 16 Thermal stress model in welding of glass by **a** CW-laser (molten pool has free surface) and **b** USLP (molten pool is embedded). *Length of each bar* drawn in the figure indicates the situation without connecting to the rigid body. *Orange* and *red colors* show the region heated to temperatures below and above T_M, respectively. *Plus* and *minus* represent tensile and compressive stress, respectively
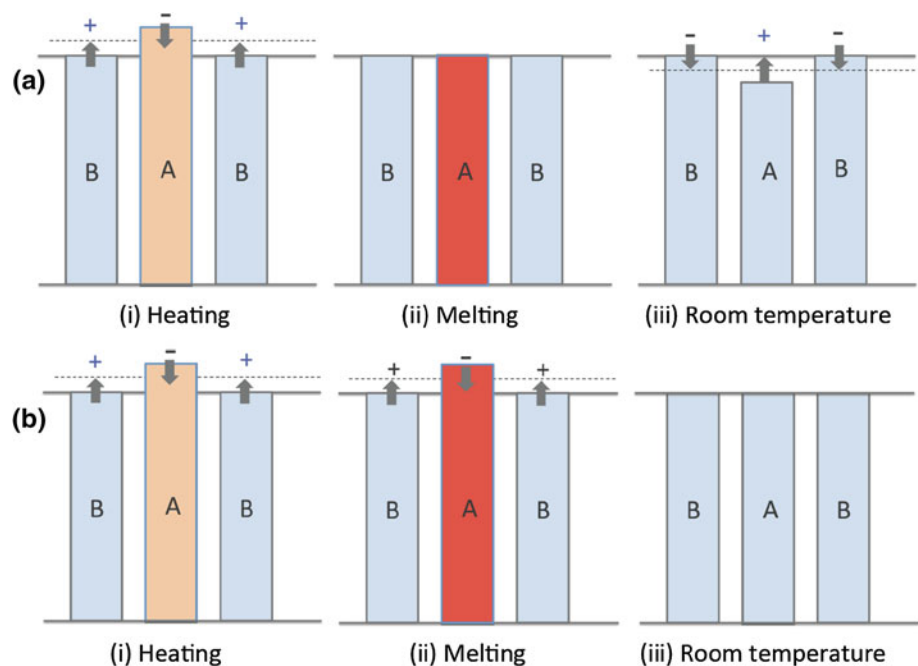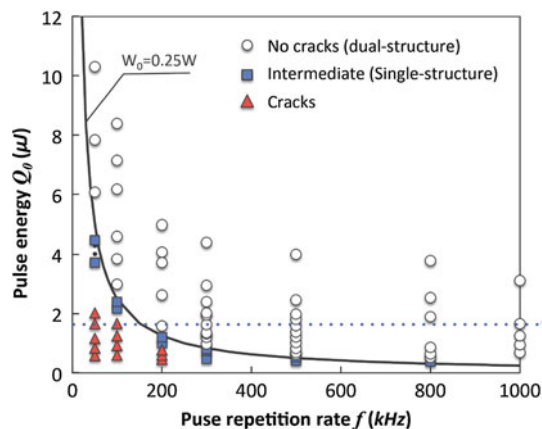
Fig. 17 Conditions of crack-free (*open circle*), cracking (*triangle*) and intermediate (*square*) at $v = 20$ mm/s in D263. Crack-free internal melting is available at average laser powers $W > W_{cr} \approx 0.25$ W. Cross-sections along the *dotted line* are shown in Fig. 8

molten pool has free surface. In cooling process after solidification of the molten region, the thermal shrinkage occurs in bar A, and is constrained by bar B (iii) so that tensile and compressive stresses are produced in bars A and B, respectively. At room temperature, cracks are produced in bar A if the tensile stress in bar A exceeds the material strength because glass has no ductility at room temperature. Thus crack-free welding is available only in glass having small CTE like fused silica [33]. This is well-known process producing shrinkage stress, which makes crack-free welding with CW-laser impossible.

The thermal stress in USLP welding of glass is shown in Fig. 16b. In heating process, the tensile stress is produced in bar B like the case of CW-laser welding. However, no temperature rise occurs in bar B in the heating process, since the pulse duration of USLP is too short for the thermal conduction from bar A to bar B to occur (i). Therefore whether or not cracks are produced depends on the temperature of bar B at the moment of the impingement of the laser pulse. The tendency for cracking is higher in single pulse irradiation than successive laser pulses, because bar B does not have ductility at the moment of the pulse impingement. At high pulse repetition rates, cracks in bar B can be prevented, since the temperature of bar B reaches higher temperature to gain ductility due to heat accumulation.

When bar A is melted, the situation is completely different from CW-laser welding, because an embedded molten pool is produced by nonlinear absorption process. USLP produces the special molten pool having no free surface, which is different from usual molten pool having free surface encountered in CW-laser welding, because the USLP energy is absorbed in the bulk glass by nonlinear process. It should be noted that the embedded molten pool cannot be plastically

deformed, despite the fact that the glass itself is plastic at temperatures $T > T_M$. Thus the embedded molten pool behaves like an elastic body (ii) in contrast to the molten pool having free surface in CW-laser welding. Therefore no plastic deformation occurs in bar A during melting, and hence no thermal stress is left in bars A and B when bar A is cooled down to room temperature (iii), because the elastic strain is reversible. Therefore crack-free welding is realized even in glass having large CTE.
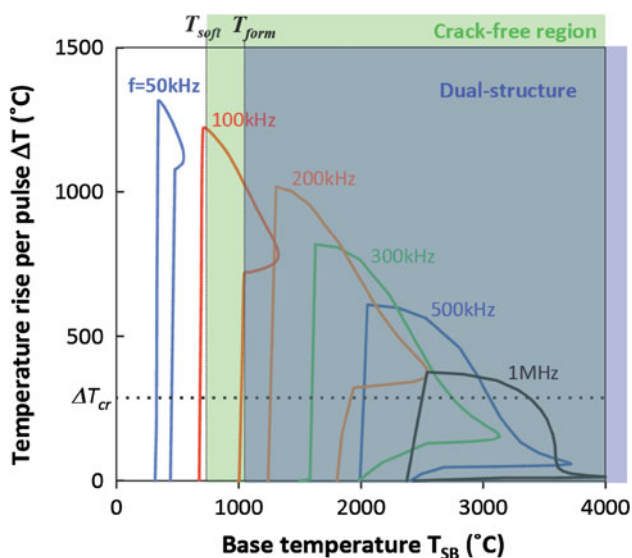
3.2.2 Crack-free condition in heating process in USLP welding

The tendency for cracking is larger in heating process in USLP welding than in CW-laser welding, because the energy of USLP is deposited instantaneously. However, cracks can be suppressed at high pulse repetition rates. Here the crack-free condition in heating process by USLP in bulk D263 is determined at different pulse energies and pulse repetition rates using 10 ps-laser pulse at $v = 20$ mm/s. Figure 17 shows the crack-free conditions at steady state ($N \to \infty$), where the cross-sections are shown in Figs. 2 and 8. Here the crack-free condition only in heating process is discussed, and the cooling process is discussed later. As seen in Fig. 17, cracks are produced at average laser powers lower than a critical value of $W_{cr} \approx 0.25$ W. Qualitatively this is understandable, because some average laser power is needed to develop temperature field to make the surrounding region (bar B) ductile.

It will be reasonable to assume that ΔT and T_{SB} in Eqs. (11) and (12) are the measures of the thermal shock and ductility of glass, respectively. Then the tendency for cracking can be qualitatively estimated from $\Delta T - T_{SB}$ diagram. ΔT and T_{SB} along the laser axis are simulated at pulse energy of $Q_0 = 1.67$ μJ (dotted line in Fig. 17) at different pulse repetition rates where the cross-sections are shown in Fig. 8a. Figure 18 shows the relationship between ΔT and T_{SB} produced by the re-plot of Fig. 11. As the pulse repetition rate f increases, the minimum of T_{SB} increases, and the peak of ΔT decreases, indicating the tendency for cracking decreases. It is also seen that ΔT increases and T_{SB} decreases as the focus is approached, suggesting the tendency for cracking increases near the focus.

If bar B has no ductility, the critical temperature rise due to the laser pulse for producing cracks in bar B is given by $\Delta T_{cr} = \sigma/\alpha_{cte}E$ [35] where $\sigma =$ material strength, $\alpha_{cte} =$ CTE and $E =$ Young's modulus. Using $\sigma = 150$ MPa [27, 67], $E = 7.3 \times 10^4$ MPa and $\alpha_{cte} = 7.2 \times 10^{-6}/°C$ in D263, ΔT_{cr} is estimated to be as low as $\Delta T_{cr} \approx 285$ °C.

Since ΔT is normally larger than ΔT_{cr} in internal melting of glass as shown in Fig. 18, crack-free condition in heating process is in fact given by

Fig. 18 Relationship between ΔT and $T_{SB}(z)$ at $Q_0 = 1.67$ μJ at different pulse repetition rates in D263 at steady state ($N \to \infty$). The region highlighted by *green* and *blue colors* correspond to the crack-free condition in heating process and dual-structure, respectively

$$T_{SB}(z) > T_{soft} \tag{14}$$

whose region is highlighted with *green color*.

At $f = 50$ kHz and $Q_0 = 1.67$ μJ, the simulated base temperature is in a range of $T_{SB} = 320$–440 °C, which is significantly lower than softening temperature of D263 $T_{soft} = 736$ °C, while $\Delta T = 1{,}300$ °C is much higher than ΔT_{cr}, corresponding to cracking condition in Fig. 18. Accordingly large cracks are actually produced above and below the laser-irradiated region as shown Fig. 8.

At $f = 100$ kHz, while the minimum of T_{SB} is slightly lower than T_{soft} near the focus, the peak of ΔT is significantly higher than ΔT_{cr}, showing crack-free condition is only partially fulfilled. In accordance with this result, a small crack is found near the focus as is seen in Fig. 8.

At $f \geq 200$ kHz where dual structure is produced as seen in Fig. 8, the crack-free condition, Eq. (14), is safely fulfilled in the whole laser-absorption region. In this condition, T_{SB} is higher than not only T_{soft} but even forming temperature T_{form}. The dual-structure is a visual sign of crack-free condition, which guarantees crack-free internal melting more safely than the green region, since the laser-absorption region (inner structure) is completely surrounded by the molten region (the outer structure). In Fig. 18, the region corresponding to dual-structure is highlighted by blue color.

Internal modification with the dual-structure has been reported in a plenty of papers where USLP of fs to ps regimes is used for different glasses having large α_{cte}, which include D263 ($\alpha_{cte} = 7.2 \times 10^{-6}$/°C) [27, 31, 32], 0211 ($\alpha_{cte} = 7.4 \times 10^{-6}$/°C: Corning) [13, 48], AF45
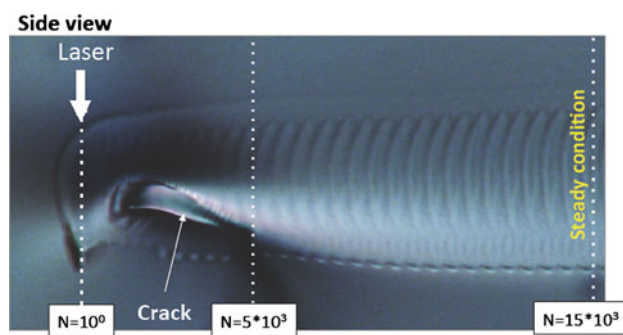
Fig. 19 Side view of laser-irradiated region at $Q_0 = 2.4$ μJ at $f = 1$ MHz in D263. N shows the number of laser pulse from the beginning

($\alpha_{cte} = 4.5 \times 10^{-6}$/°C: Schott) [15, 28], B270 ($\alpha_{cte} = 9.4 \times 10^{-6}$/°C: Schott) [29, 30], Foturan ($\alpha_{cte} = 8.6 \times 10^{-6}$/°C: Schott) [24], and Eagle 2000 ($\alpha_{cte} = 3.18 \times 10^{-6}$/°C: Corning) [19]. No cracks are found in these cross-sections, supporting out model.

The thermal stress analyzed in Fig. 18 is at steady state. However, the tendency for cracking increases significantly at the beginning of the laser irradiation where $T_{NB}(z)$ does not reach steady value at $N < N_S$ shown in Fig. 10. Figure 19 shows an example of the side view at 20 mm/s at $Q_0 = 2.4$ μJ and $f = 1$ MHz, which corresponds to crack-free region at steady state ($N \to \infty$) in Fig. 17. In this case, cracks are observed between $N = 10^0$ and $N = 5 \times 10^3$, because $T_{NB}(z)$ is still lower than T_{soft}.

3.2.3 Crack-free condition in cooling process in USLP welding

In order to demonstrate the visual evidence to support the model where crack-free welding needs embedded molten pool in Fig. 16b, two experiments were conducted at 1 MHz at 2.4 μJ, which corresponds to crack-free region in heating process in Fig. 17.

Firstly, 10 ps-laser pulses were focused near the rear surface of the tilted glass plate, and the sample was moved horizontally as shown in Fig. 20a. Appearance of the molten region near the bottom surface is shown in Fig. 20b. While no cracks are found when the molten pool is embedded in bulk glass (region i), cracks are produced when the molten region is exposed to the bottom surface (region ii).

Secondly, two glass plates with optical contact was cramped mechanically on one side and a metallic foil with a thickness of 30 μm was inserted from the other side to provide the sample pair having varying clearance d between glass plates as shown in Fig. 21a. Welding was performed using 10 ps-laser pulses. Figure 21b shows the top view of the molten region illuminated by the light of
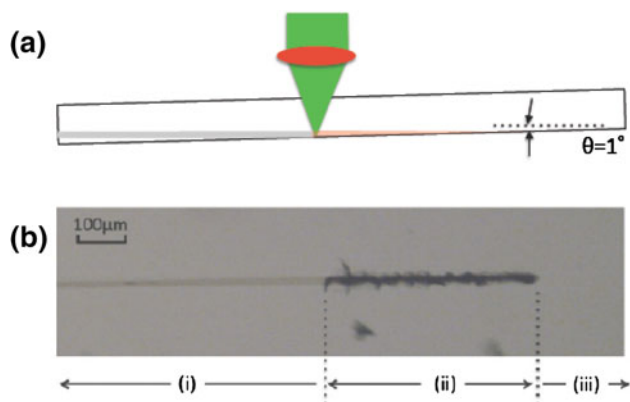
Fig. 20 **a** Experimental set up of tilted plate sample with focus near the bottom surface. **b** Laser-irradiated region for tilted sample ($f = 1$ MHz, $Q_0 = 1.6$ µJ) *i* crack-free internal melting, *ii* cracks produced in molten region that is exposed to the surface and *iii* no melting
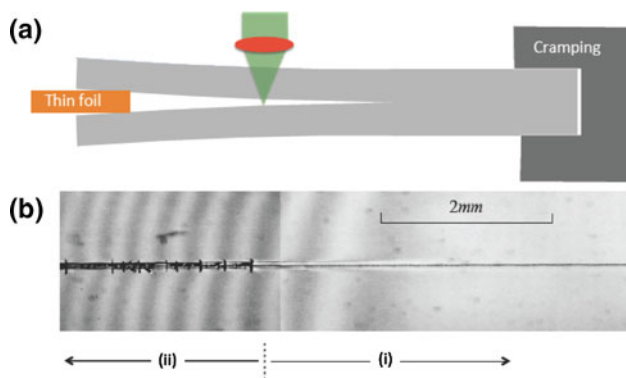
Fig. 21 **a** Experimental set up for overlap-welding with varied gap distance between glass plates. **b** Top view of overlap-welded D263 sample irradiated by *green light* ($\lambda = 530$ nm)

530 nm. When the clearance d is larger than a critical value of d_c of the order of a hundred nm, cracks are produced. This is because the molten glass has flowed out of the molten region (plastic deformation) by the compressive stress produced in the heating process, so that the thermal stress is released as in the case of (i) in Fig. 16a. As a result, tensile stress is produced after cooling down to room temperature to produce cracks in bar A. However, at conditions of $d < d_c$, no cracks are produced, since the amount of molten glass flowing out of the molten region during melting period is limited by the viscous resistance. At $d > d_c$, the viscous resistance of the molten glass decreases as d increases, and hence larger amount of molten glass flows out so that larger shrinkage stress is produced after cooing down to room temperature to produce cracks. It should be emphasized that even if cracks are not produced, the joint strength should be reduced by the residual tensile stress if the molten glass, more or less, flows out. This is the reason why we
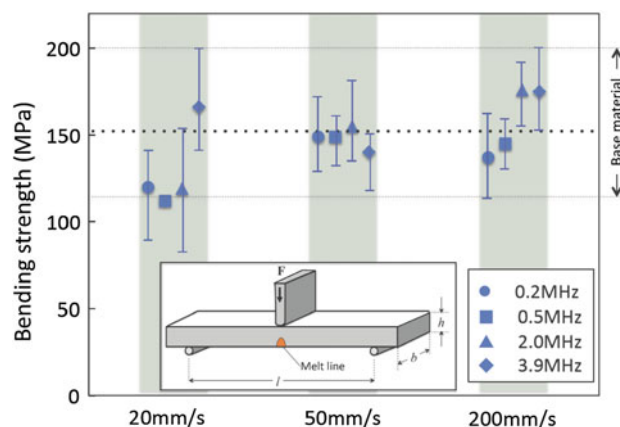
Fig. 22 Mechanical strength of internally melted single Foturan sample determined by a three-point-bending test at different f and v at a constant average laser power of 2.5 W. *Inset* shows the arrangement of the three-point-bending test

strongly recommend the optical contact to obtain weld joint with high mechanical strength.

3.3 Mechanical strength of weld joint

3.3.1 Mechanical strength of internally melted single sample

Mechanical strength of weld joint is not easy to evaluate exactly, because it is affected not only by the laser parameters for welding, but by the geometry of the weld joint, the testing method and so on. So prior to evaluating the strength of the weld joint, the effect of the laser parameters on the mechanical strength was evaluated with the internally melted single glass samples. While the mechanical properties of the internally modified glass samples have been examined by different testing procedures including a four-point-bending test [68], a double torsion test [69] and nano-indentation [70, 71], a three-point-bending test is used in this study.

Photosensitive ceramic glass sample of Foturan (Schott) with a thickness of 1.1 mm was internally melted at an average laser power of 2.5 W at different pulse repetition rates f and the translation speeds v using 10 ps-laser pulses. The internally melted glass samples were lapped and polished to expose the maximum width of the molten region to the surface, and then cut perpendicularly to the melt line. The three-point-bending test was performed with applying the maximum stress at the molten region (see the inset of Fig. 22), and the mechanical strength of the molten region σ was determined by

$$\sigma = \frac{3Fl}{2bh^2} \tag{15}$$

The bending strength of the virgin material with no laser irradiation dose falls within the region of 115–200 MPa

(average strength 152 MPa) as seen in Fig. 22. On the other hand, the average value of all the internally melted samples (60 data points in total) is approximately 145 MPa, nearly equivalent to the base material. The bending strength exhibits a tendency to increase as the pulse repetition rate f increases. This is because bar B gains more ductility due to higher temperature at the moment of the laser pulse impingement by the heat accumulation at higher pulse repetition rates. It is noted that the bending strength of the internally melted samples can be as high as or even above that of the base material.

The data shown in Fig. 22 are re-plotted in Fig. 23 as a function of the average absorbed laser power W_{ab} determined by Eq. (10). It is seen that all the data fall on the zone highlighted by the blue-colored region. While the mechanical strength decreases with increasing W_{ab}, there is a possibility of even strengthening the material beyond the base material in the region $W_{ab} < 1.0$ W. This result is supported by our previous report where the internally melted single plate of fused silica by USLP can be stronger than that of the base material [67].

3.3.2 Mechanical strength of welded joint

Mechanical strength of the welded joint by USLP has been evaluated by a variety of methods including a tensile test [10, 11], a three-point bending test [25, 26] and a shear test [24, 27, 49]. In the present study, a shear test was adopted for evaluating overlap weld joint strength.

Based on the aforementioned thermal stress analysis, optical contact for sample preparation is recommended to provide strong weld joint for the sample preparation, because the mechanical strength of the weld joint without optical contact is decreased by the residual tensile stress. The optical contact is marked by a lack of light reflections
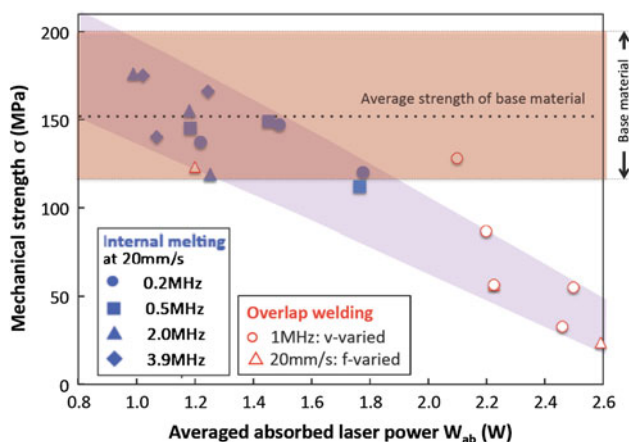
from the interface with low roughness and high flatness, and is normally obtained with commercially available float glass, if the glass surfaces are carefully cleaned [64]. Lapping and polishing are, however, needed to provide optical contact in the case of Foturan glass plates, since the surface roughness and flatness of as-received Foturan glass plates are not high enough. Foturan sample pairs in optical contact are overlap-welded by irradiating the tightly focused 10 ps-laser pulses. The focus position is located a little below the interface so that the interface of the glass pieces intersects the molten region at its maximum width.

In evaluating the mechanical strength of the weld joint by the shear test, the effect of the optical contact force on the shear strength has to be subtracted. The optical contact force is caused by van der Waals interactions between the glass pieces [63], and can be evaluated by measuring the shear force to break the optical contact of the sample without weld bead. Glass samples of a 15 mm width with different lengths L were used for this purpose. Figure 24 shows the shear force F_{OC} to break the optical contact plotted as a function of optical contact area S_{OC}. The optical contact force per unit area σ_{OC} ($=F_{OC}/S_{OC}$) is approximately 1.5 MPa at $L = 1$ mm, and decreases with increasing S_{OC}. The values of σ_{OC} in $S_{OC} < 200$ mm^2 are in agreement with the values reported for glass materials by Kachkin et al. [72].

Overlap welding was performed using the sample pre-bonded by optical contact with $L = 10$ mm corresponding to $F_{OC} \approx 88.2$ N ($\sigma_{OC} \approx 0.6$ MPa), which is strong enough to keep optical contact in handling the sample for the welding experiment. Although $\sigma_{OC} \approx 0.6$ MPa is approximately two orders smaller than the strength of Foturan glass, $L = 10$ mm is also two orders larger than typical bead width. Therefore the strength of the weld joint σ_W was determined by subtracting the optical contact force F_{OC} from the rupture load F_{RUP}, and then dividing by the cross-sectional area of the weld bead S_W using
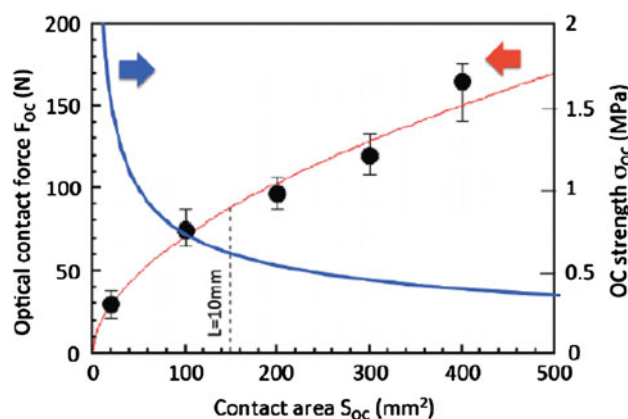

Fig. 23 Mechanical strength of internally melted single glass sample (three-point-bending test) and overlap-welded joint (shear test) plotted vs. average absorbed laser power W_{ab}


Fig. 24 Shear force to break optical contact F_{OC} plotted vs. optical contact area S_{OC}. The optical contact force per unit area σ_{OC} is also plotted

$$\sigma_{\mathrm{W}} = \frac{F_{\mathrm{RUP}} - F_{\mathrm{OC}}}{S_{\mathrm{W}}}. \qquad (16)$$

Overlap welding was performed at an average laser power of 3 W at different pulse repetition rates and different translation speeds. In Fig. 25a and b, the rupture load F_{RUP} and the welded area S_{W} are plotted as a function of translation speed v at a constant pulse repetition rate of $f = 1$ MHz, and as a function of pulse repetition rate at a constant speed of $v = 20$ mm/s, respectively.

In Fig. 23, σ_{W} data for overlap-welded samples for $f = 1$ MHz and $v = 20$ mm/s are also plotted. Most data points of the overlap welding are included within the blue-colored region that highlights the data for the internal melting of the single plate studies except for one single data point taken at translation speed of 100 mm/s.

It is known since many years ago that the strength of the weld joint evaluated by $\sigma_{\mathrm{W}} = F_{\mathrm{RUP}}/S_{\mathrm{W}}$ tends to decrease as S_{W} increases, even in the case the weld bead has the same metallurgical properties. This is considered to be because the stress in the weld joint propagates not uniformly but more or less concentrates in some part of the
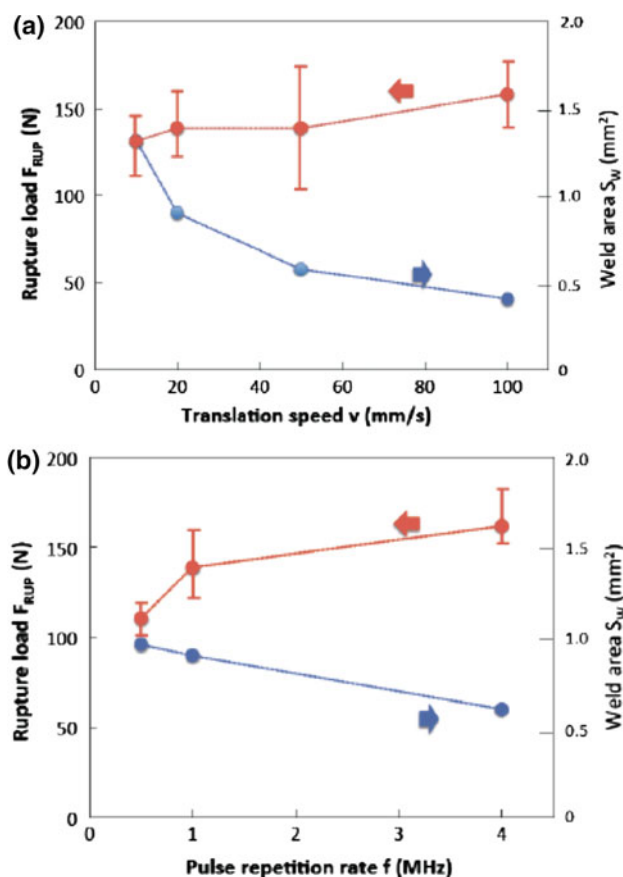
Fig. 25 Effect of **a** translation speed ($f = 1$ MHz) and **b** pulse repetition rate ($v = 20$ mm/s) on the rupture strength and weld area of the overlap-weld samples ($L = 10$ mm, length of weld path = 8–9 mm)

weld joint [34], making the comparison of the strength of the weld joint having different geometry difficult. Nevertheless the data obtained by two different mechanical tests fall on the same highlighted region, suggesting the diagonally right down tendency in Fig. 23 is valid.

3.4 Welding characteristics of Si/glass by USLP

Silicon/glass is one of the most widely used material combinations for sensing and actuating microsystem technologies. Anodic bonding has been extensively accepted for Si/glass joining in a variety of applications [73, 74] since its invention in 1968 [75] due to excellent mechanical properties and high process throughput. In anodic bonding, however, there are some disadvantages that long heating time at high temperature with high electric field is needed and space selective joining is not available.

In order to overcome the disadvantages of the anodic bonding, different types of laser-based joining techniques using ns-laser pulses have been developed, which includes eutectic bonding [76, 77], selective bonding with laser (SLB) [78, 79] and fusion welding [80, 81] as shown in Table 2. However, the performances of these joining procedures are far behind the anodic bonding in terms of mechanical strength of the joint and process throughput. While several papers have been also published on Si/glass joining using USLP [22, 82] where tightly focused fs-laser pulses are irradiated into the bulk glass to produce filament [83, 84], satisfactory joint strength and process throughput have not been reached, since sufficient laser energy is not deposited to the Si substrate due to the consumption of the laser energy at the filament in the bulk glass. In the present study, ps-laser pulse with intensity below the threshold of multiphoton ionization of glass [53, 54] is used to deposit the laser energy preferentially to Si substrate, since thermal conductivity of Si is at least two order higher than that of glass.

To begin with, welding process is compared between ns- and ps-laser pulses. Figure 26 shows the appearances of the optically contacted Si/glass sample irradiated by ns- and ps-laser pulses. Significant splash of the molten Si is observed with ns-laser pulses, suggesting the surface of Si substrate is heated above its boiling temperature so that the molten Si is removed from the laser-irradiated region by the recoil pressure of the evaporation [59]. Actually cross-section shows some clearance between the substrates (not shown here). This is because the absorption coefficient in Si substrate increases rapidly with increasing temperature, while it is rather small at room temperature [85, 86]. Thus once appreciable temperature rise at the substrate surface occurs at the leading edge of the laser pulse, the laser absorption in the second half of the laser pulse concentrates increasingly at a very thin surface layer due to local

Table 2 Comparison of Si/glass joining technologies

Joining technique			Through-put	Joint strength	Space selectivity	Comments
Anodic bonding			◎	◎	×	Heating and electric fields are needed
Laser-based joining	ns	Eutectic bonding	△	○	◎	Metal foil insertion is needed [76, 77]
		SLB	△	○	◎	Chemical treatment is needed [78, 79]
		Fusion welding	×	×	◎	[80, 81]
	fs	Fusion welding	×	×	◎	[11, 82]
	ps	Fusion welding	◎	◎	◎	Present study

◎ excellent, ○ good, △ fair, × bad
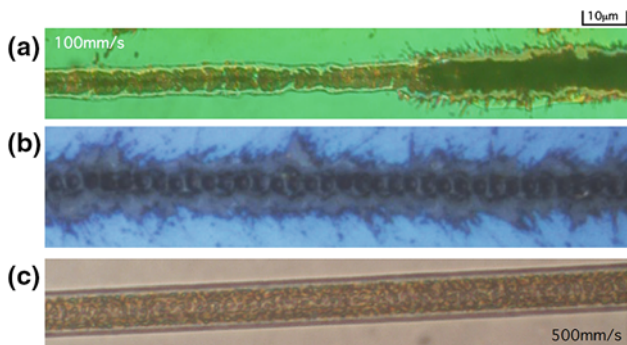
Fig. 26 Appearance of overlap-welded Si/glass sample using laser pulses with duration of **a** 12 ns ($\lambda = 1{,}046$ nm), **b** 7 ns ($\lambda = 532$ nm) and **c** 20 ps ($\lambda = 1{,}064$ nm)

Fig. 27 Shear strength of overlap-welded Si/glass joint vs. number of laser pulse in the laser spot N
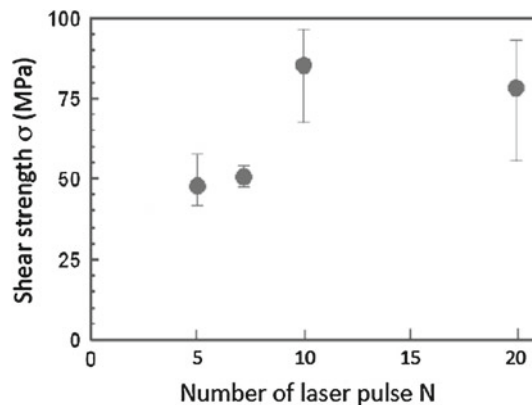
increase in the absorption coefficient. Thus it is concluded that the splash of the molten Si is caused by the temperature rise during the ns-laser pulse.

In ps-laser pulse, on the other hand, the Si/glass joint shows much smooth appearance without the splash of molten Si, indicating Si substrate is heated mildly. This is because the laser energy absorbed by free electrons is transferred to the lattice after the laser pulse in ps-regime, and hence the temperature rise of the Si substrate is delayed after the laser pulse. As the result, the laser energy penetrates deeper into the Si substrate to make heating of the Si substrate milder, since the absorption coefficient is kept smaller during the laser pulse.

Si/glass welding was performed using 20 ps-laser pulse at different translation speeds at $f = 1$ MHz and $Q_0 = 3$ μJ, which is focused by a lens of NA 0.1. Then the shear strength of the weld joint was determined based on Eq. (16). In the welding experiment, SW-Y (ATG, Japan) was used, whose CTE is very close to Si in a wide temperature range. Figure 27 shows the joint strength plotted vs. number of laser pulse in the laser spot N, which is given by

$$N = \frac{df}{v} \tag{17}$$

where $d =$ laser spot size, $f =$ pulse repetition rate and $v =$ translation speed. The joint strength, which is below

50 MPa at $N \approx 5$, increases as N increases reaching maximum value of approximately 85 MPa at $N \approx 10$. Then the joint strength tends to decrease by the further increase in N.

Figure 28 shows the cross-section of laser-welded Si/glass sample with $N \approx 10$. Interestingly, the laser-welded Si/glass interface is not flat but of intricate structure, indicating that local convection of molten Si occurs at the interface, and the glass substrate is heated by the convection. It is believed that the joint strength is increased by the anchor effect of the intricate structure.

It is noted the flow pattern of the molten Si is curved toward the laser axis in the glass region, suggesting that lower viscosity and hence higher temperature are reached near the laser axis. This is considered to be because the glass substrate is heated not only by the melt convection but direct absorption of the laser energy by avalanche ionization.

The welding process is explained as follows. The laser energy passed through the glass substrate is first absorbed in Si substrate since the laser intensity is below the threshold of MPI for the glass, and thereafter the glass substrate is indirectly heated by the melt convection and the conduction from the Si substrate. When the glass substrate is heated indirectly by conduction and convection,
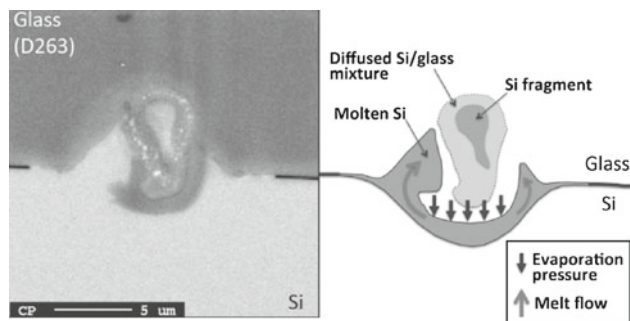
Fig. 28 *Left* SEM photograph showing cross-section of laser-welded Si/D263 ($f = 2$ MHz, $Q_0 = 2$ μJ, $v = 2$ m/s). *Right* schematic illustration showing the process of intricate structure produced by the recoil pressure for evaporation

Fig. 29 Laser-welded grid pattern in Si/Pyrex at $f = 2$ MHz, $Q_0 = 1$ μJ and $v = 200$ mm/s. Weld line of width 180 μm consists of 20 weld lines. **a** Appearance of diced sample. **b** Magnified picture of diced sample

and thereby the thermally excited free electron density in the glass substrate becomes high enough, the glass substrate is directly heated also by the laser absorption via avalanche ionization. The direct laser absorption is strengthened by the decreased band gap caused by the Si/glass mixture, enabling avalanche ionization without seeding free electrons by photoionization. Further increase in N decreases the joint strength, because the laser energy reaching the interface is decreased by the excess absorption in the glass region.

The USLP welding of Si/glass provides significantly higher throughput than the existing laser-based joining procedures, and can compete even with anodic bonding. The throughput of Si/glass welding A_W by USLP can be defined by:

$$A_W = \Delta_s f D \tag{18}$$

where Δ_S = displacement of laser spot per pulse and D = bead width. A_W increases proportionally to pulse repetition rate, since no instability of the molten pool occurs at high welding speed in embedded molten pool, unlike the case of existing metal welding having free surface where the welding speed is limited by the instability of the molten pool [59]. The attainable value of the throughput A_W is as large as 60 mm²/s at $f = 4$ MHz, for instance, at $\Delta_S = 1$ μm ($N \approx 10$, $D = 15$ μm). This means that whole area of silicon wafer of 6 in., for instance, can be completely bonded to glass substrate within 5 min. When considering that the USLP welding technique does not need pre-heating and post-heating at all, the joining rate of this technique is fast enough to compete with anodic bonding in terms of throughput. Higher throughput can be attained at higher pulse repetition rates using laser beam scanner with higher scanning speeds.

One of the distinguished advantages of Si/glass welding by USLP is its excellent space selectivity. The spatial resolution of the weld line of approximately as small as 10–15 μm is available as seen in Fig. 26. In order to
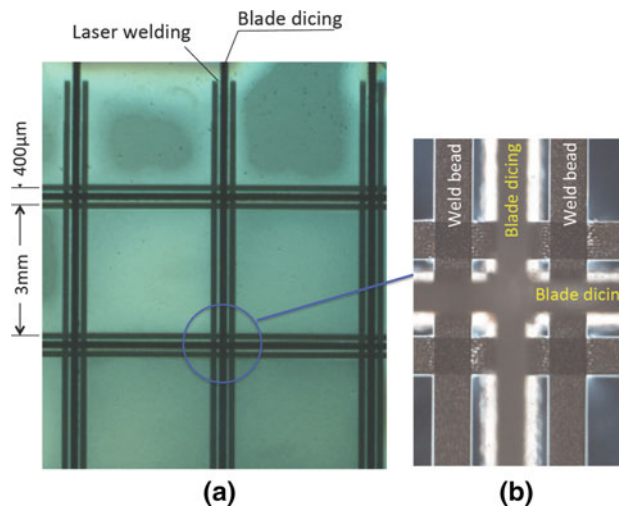
demonstrate the advantage of the space selectivity in Si/glass joining, a grid-geometry with a size of 3 mm having a street width of 400 μm shown in Fig. 29 was "drawn" by the laser welding lines in joining Si/Pyrex sample. Each weld line with a width of 180 μm consists of 20 weld lines. No defects are found at the interface of Si and Pyrex substrates by ultrasonic test and the observation by the optical microscope. The laser-welded samples were cut by a standard blade dicer along the street. No defects are produced without coolant passage through the welded line by dicing, showing the weld joint has excellent mechanical strength and hermetic properties for packaging, MEMS, sensors and so on.

An accelerated life test (500 cycles between −40 and 85 °C) was also performed using laser-welded silicon-Borofloat 33 sample (Schott). No damage is found with keeping hermetic sealing, showing possibility of versatile applications.

References

1. K.M. Davis, K. Miura, N. Sugimoto, K. Hirao, Opt. Lett. **21**, 1729 (1996)
2. K. Miura, J. Qiu, H. Inouye, T. Mitsuyu, K. Hirao, Appl. Phys. Lett. **71**, 3329 (1997)
3. A.M. Streltsov, N.F. Borrelli, J. Opt. Soc. Am. B **19**, 2496 (2002)
4. D.J. Little, M. Ams, P. Dekker, G.D. Marshall, J.M. Dawes, M.J. Withford, Opt. Express **13**, 20029 (2008)

5. D. Homoelle, S. Wielandy, A.L. Gaeta, N.F. Borrelli, C. Smith, Opt. Lett. **24**, 1311 (1999)
6. K. Minoshima, A.M. Kowalevicz, I. Hartl, E.P. Ippen, J.G. Fujimoto, Opt. Lett. **26**, 1516 (2001)
7. H. Zhang, S.M. Eaton, J. Li, A.H. Nejadmalayeri, P.R. Herman, Opt. Express **15**, 4182 (2007)
8. S. Juodkazis, H. Misawa, I. Maksimov, Appl. Phys. Lett. **85**, 5239 (2004)
9. C. Hnatovsky, R.S. Taylor, E. Simova, V.R. Bhardwaj, D.M. Rayner, P.B. Corkum, Opt. Lett. **30**, 1867 (2005)
10. T. Tamaki, W. Watanabe, J. Nishii, K. Itoh, Jpn. J. Appl. Phys. **44**, L687 (2005)
11. W. Watanabe, S. Onda, T. Tamaki, K. Itoh, J. Nishii, Appl. Phys. Lett. **89**, 021106 (2006)
12. I. Miyamoto, A. Horn, J. Gottmann, J. Laser Micro/Nanoeng **2**, 7 (2007)
13. C.B. Schaffer, J.F. Garcia, E. Mazur, Appl. Phys. A **76**, 351 (2003)
14. C.B. Schaffer, A. Brodeur, J.F. Garcia, E. Mazur, Opt. Lett. **26**, 93 (2001)
15. S. Nolte, M. Will, J. Burghoff, A. Tünnermann, J. Mod. Opt. **51**, 2533 (2004)
16. L. Shah, A.Y. Arai, S.M. Eaton, P.R. Herman, Opt. Express **13**, 1999 (2005)
17. R. Osellame, N. Chiodo, V. Maselli, A. Yin, M. Zavelani-Rossi, G. Cerullo, P. Laporta, L. Aiello, S. De Nicola, P. Ferraro, A. Finizio, G. Pierattini, Opt. Express **13**, 612 (2005)
18. S.M. Eaton, H. Zhang, M.L. Ng, J. Li, W.J. Chen, S. Ho, P.R. Herman, Opt. Express **16**, 9443 (2008)
19. A. Arriola, S. Gross, N. Jovanovic, N. Charles, P.G. Tuthill, S.M. Olaizola, A. Fuerbach, M.J. Withford, Opt. Express **21**, 2978 (2013)
20. J. Gottmann, M. Hermans, J. Ortmann, Phys. Procedia **39**, 534 (2012)
21. Y. Bellouard, A. Champion, B. Lenssen, M. Matteucci, A. Schaap, M. Beresna, C. Corbari, M. Gecevicius, P. Kazansky, O. Chappuis, M. Kral, R. Clavel, F. Barrot, J.M. Breguet, Y. Mabillard, S. Bottinelli, M. Hopper, C. Hoenninger, E. Mottay, J. Lopez, J. Laser Micro/Nanoeng **7**, 1 (2012)
22. T. Tamaki, W. Watanabe, K. Itoh, Opt. Express **14**, 10468 (2006)
23. I. Miyamoto, A. Horn, J. Gottmann, D. Wortmann, F. Yoshino, J. Laser Micro/Nanoeng **2**, 57 (2007)
24. I. Miyamoto, K. Cvecek, Y. Okamoto, M. Schmidt, H. Helvajian, Opt. Express **19**, 22961 (2011)
25. S. Richter, S. Doring, A. Tunnermann, S. Nolte, Appl. Phys. A **103**, 257 (2011)
26. F. Zimmermann, S. Richter, S. Döring, A. Tunnermann, S. Nolte, Appl. Opt. **52**, 1149 (2013)
27. Y. Okamoto, I. Miyamoto, K. Cvecek, A. Okada, K. Takahashi, M. Schmidt, J. Laser Micro/Nanoeng **8**, 65 (2013)
28. S.M. Eaton, H. Zhang, P.R. Herman, F. Yoshino, L. Shah, J. Bovastek, A.Y. Arai, Opt. Express **13**, 4708 (2005)
29. M. Sakakura, M. Shimizu, Y. Shimotsuma, K. Miura, K. Hirao, Appl. Phys. Lett. **93**, 231112 (2008)
30. M. Shimizu, M. Sakakura, M. Ohnishi, M. Yanaji, Y. Shimotsuma, K. Hirao, K. Miura, Opt. Express **20**, 934 (2012)
31. I. Miyamoto, K. Cvecek, M. Schmid, Opt. Express **19**, 10714 (2011)
32. I. Miyamoto, K. Cvecek, M. Schmidt, Opt. Express **21**, 14291 (2013)
33. Y. Arata, H. Maruo, I. Miyamoto, S. Tackuchi, Proc. Symp. Electron Ion Beam Sci. Technol. **7**, 111 (1976)
34. M. Watanabe, K. Satoh, in *Welding mechanics and its applications* (Asakura, 1965), chap. 8
35. T. Terasaki, J. Jpn. Weld. Soc. **78**, 139 (2009)
36. K. Nahen, A. Vogel, J. Sel. Topics Quant. Electron. **2**, 861 (1996)
37. K. Sugioka, M. Iida, H. Takai, K. Midorikawa, Opt. Lett. **36**, 2734 (2011)
38. S. Wu, D. Wu, J. Xu, Y. Hanada, R. Suganuma, H. Wang, T. Makimura, K. Sugioka, K. Midorikawa, Opt. Express **20**, 28893 (2012)
39. T. Yoshino, Y. Ozeki, M. Matsumoto, K. Itoh, Jpn. J. Appl. Phys. **51**, 102403 (2012)
40. F. Hashimoto, S. Richter, S. Nolte, Y. Ozeki, K. Itoh, in *Proceeding of the 6th international congress on laser advanced materials processing*, 2013
41. A. Vogel, K. Nahen, D. Theisen, J. Noack, IEEE J. Quantum Electron. **4**, 847 (1996)
42. Y.R. Shen, *The Principles of Nonlinear Optics* (Wiley, New York, 1984)
43. J. Noack, A. Vogel, IEEE J. Quantum Electron. **35**, 1156 (1999)
44. C.L. Arnold, A. Heisterkamp, W. Ertmer, H. Lubatschowski, Opt. Express **15**, 10303 (2007)
45. H.S. Carslaw, J.C. Jaeger, *Conduction of Heat in Solids* (Clarendon, Oxford, 1959)
46. A.E. Siegman, S.W. Townsent, IEEE J. Quantum Electron. **29**, 1212 (1993)
47. Y. Liu, M. Shimizu, B. Zhu, Y. Dai, B. Qian, J. Qiu, Y. Shimotsuma, K. Miura, K. Hirao, Opt. Lett. **34**, 136 (2009)
48. J. Bovatsek, A. Araia, C.B. Schaffer, in *Proceeding of the CLEO/Europe—EQEC2005*, vol. 1, 2005
49. K. Cvecek, I. Miyamoto, J. Strauss, M. Wolf, T. Frick, M. Schmidt, Appl. Opt. **50**, 1941 (2011)
50. A.K. Varshneya, *Fundamentals of Inorganic Glasses* (Academic, Boston, 1994)
51. P.K. Kennedy, IEEE J. Quantum Electron. **31**, 2241 (1995)
52. K. Morigaki, *Physics of Amorphous Semiconductors* (Imperial College Press, 1999)
53. D. Du, X. Liu, G. Korn, J. Squier, G. Mourou, Appl. Phys. Lett. **64**, 3071 (1994)
54. B.C. Stuart, M.D. Feit, S. Herman, A.M. Rubenchik, B.W. Shore, M.D. Perry, Phys. Rev. B **53**, 1749 (1996)
55. H. Behrens, M. Haack, J. Non Cryst. Solids **353**, 4743 (2007)
56. M. Sun, U. Eppelt, W. Schulz, J. Zhu, Opt. Mater. Express **3**, 1716 (2013)
57. M. Tavakoli, *The Adhesive Bonding of Medical Devices* (Medical Devices & Diagnostics Industry, 2001)
58. B.G. Yacobi, S. Martin, K. Davis, A. Hudson, M. Hubert, J. Appl. Phys. **91**, 6227 (2002)
59. I. Miyamoto, G.A. Knorovsky, in *Laser Microwelding* ed. by Y. Zhou. Microjoining and Nanojoining (Woodhead Publishing, Cambridge, 2008)
60. M. Levesque, B. Labrnche, R. Forest, E. Savard, S. Deshaies, A. Cournoyer, Phys. Procedia **5**, 139 (2010)
61. L. Schaefer, M. Schmidt, Phys. Procedia **5**, 145 (2010)
62. W. Watanabe, T. Toma, K. Yamada, J. Nishii, K. Hayashi, K. Itoh, Opt. Lett. **25**, 1669 (2000)
63. V. Greco, F. Marchesini, G. Molesini, J. Opt. A. Pure Appl. Opt. **3**, 85–88 (2001)
64. http://labaccessories.mellesgriot.com/pdfs/Cleaning_Methods.pdf. Accessed 1 Oct 2013
65. S. Richter, S. Nolte, A. Tuennermannm, Phys. Procedia **39**, 556 (2012)
66. Y. Oki, Y. Ozeki, K. Itoh, in *Proceeding of the 12th international symposium on laser precision microprocessing* (*LPM*), 2011
67. I. Miyamoto, A. Horn, J. Gottmann, D. Wortmann, I. Mingareev, F. Yoshino, M. Schmidt, P. Bechtold, Y. Okamoto, Y. Uno, T. Herrmann, in *Proceeding of the 27th ICALEO*, 2008
68. K. Hirao, Y. Shimotsuma, J. Qiu, K. Miura, Mater. Res. Soc. Symp. Proc. **850** (2005)
69. N. Borrelli, J. Helfinstine, J. Price, J. Schroeder, A. Atreltsov, J. Westbrook, in *Proceeding of the 27th ICALEO*, 2008

70. Y. Bellouard, T. Colomb, C. Depeursinge, M. Dugan, A.A. Said, P. Bado, Opt. Express **14**, 8360 (2006)
71. P. Kongsuwan, H. Wang, S. Vukelic, Y.L. Yao, J. Manuf. Sci. Eng. **132**, 041009 (2010)
72. S.S. Kachkin, Y.V. Lisitsyn, Sov. J. Opt. Technol. **47**, 159 (1980)
73. G. Wallis, D. Pomerantz, J. Appl. Phys. **40**, 3946 (1969)
74. M. Esashi, Microsyst. Technol. **1**, 2 (1994)
75. P.R. Mallory & Co., in *Anodic Bonding*. US Patent 3 397 278 (1968)
76. Y.T. Cheng, L. Lin, J. Microelectromech. Syst. **9**, 3 (2000)
77. U.M. Mescheder, M. Alavi, K. Hiltmann, Ch. Lietzau, Ch. Nachtigall, H. Sandmaier, Sens. Actuator A **97/98**, 422 (2002)
78. M.J. Wild, A. Gillner, R. Poprawe, Sens. Actuator A **93**, 63 (2001)
79. F. Sari, M. Rupf, A. Gillner1, R. Poprawe, in *Proceeding of the 3rd WLT-conference on laser in manufacturing 2005, Munich*, 2005
80. C. Luo, L. Lin, Sens. Actuator A **97/98**, 398 (2002)
81. J.-S. Park, A.A. Tseng, in *Proceeding of the 2004 JUSFA Japan US symposium on flexible automation, Denver*, 2004
82. A. Horn, I. Mingareev, A. Werth, M. Kachel, U. Brenk, Appl. Phys. A Mater. Sci. Process. **93**, 171 (2008)
83. L. Sudrie, A. Couairon, M. Franco, B. Lamouroux, B. Prade, S. Tzortzakis, A. Mysyrowicz, Phys. Rev. Lett. **89**, 186601 (2002)
84. A. Couairona, A. Mysyrowicz, Phys. Rep. **441**, 47 (2007)
85. G.E. Jellison Jr, D.H. Lowndes, Appl. Phys. Lett. **41**, 594 (1982)
86. D. Kovalev, G. Polisski, M. Ben-Chorin, J. Diener, F. Koch, J. Appl. Phys. **80**, 5978 (1996)